

Predictive Collective Variable Discovery with Deep Bayesian Models

Markus Schöberl,^{1, 2, a)} Nicholas Zabaras,^{1, b)} and Phaedon-Stelios Koutsourelakis^{2, c)}

¹⁾ *Center for Informatics and Computational Science, University of Notre Dame, 311 Cushing Hall, Notre Dame, IN 46556, USA.*

²⁾ *Continuum Mechanics Group, Technical University of Munich, Boltzmannstraße 15, 85748 Garching, Germany.*

(Dated: 10 June 2022)

Extending spatio-temporal scale limitations of models for complex atomistic systems considered in biochemistry and materials science necessitates the development of enhanced sampling methods. The potential acceleration in exploring the configurational space by enhanced sampling methods depends on the choice of collective variables (CVs). In this work, we formulate the discovery of CVs as a Bayesian inference problem and consider the CVs as hidden generators of the full-atomistic trajectory. The ability to generate samples of the fine-scale atomistic configurations using limited training data allows us to compute estimates of observables as well as our probabilistic confidence on them. The methodology is based on emerging methodological advances in machine learning and variational inference. The discovered CVs are related to physicochemical properties which are essential for understanding mechanisms especially in unexplored complex systems. We provide a quantitative assessment of the CVs in terms of their predictive ability for alanine dipeptide (ALA-2) and ALA-15 peptide.

^{a)}Electronic mail: mschoeberl@gmail.com

^{b)}<https://cics.nd.edu/>; Electronic mail: nzabaras@gmail.com

^{c)}<http://www.contmech.mw.tum.de>; Electronic mail: p.s.koutsourelakis@tum.de

I. INTRODUCTION

Molecular dynamics (MD) simulations, in combination with prevalent algorithmic enhancements and tremendous progress in computational resources, have contributed to new insights into mechanisms and processes present in physics, chemistry, biology and engineering. However, their applicability in systems of practical relevance poses insurmountable computational difficulties in^{1,2}. For example, the simulation of $M = 10^5$ atoms over a time horizon of a mere $T \approx 10^{-4}$ s with a time step of $\Delta t = 10^{-15}$ s implies a computational time of one year³. A rugged free-energy surface and configurations separated by high free-energy barriers lead to unobserved conformations even in very long simulations.

Enhanced sampling methods⁴ provide a framework for accelerating the exploration of the configurational space^{5–11}. Those methods rely on the existence of a lower-dimensional representation of the atomistic detail. Lower-dimensional system variables (reaction coordinates), capture the characteristics of the system, allow us to understand relevant processes and conformational changes¹², and can enable guided and enhanced MD simulations. *Reaction coordinates* provide quantitative understanding of macromolecular motion, whereas *order parameters* are of qualitative nature as discussed in [13]. In the following, we use the term *collective variables* (CVs), combining the quantitative and qualitative properties of reaction coordinates and order parameters, respectively. Refs. [4 and 13] review the challenges in the exploration of the free-energy landscape and the identification of “good” collective variables.

Adding an appropriate biasing potential or force, based on CVs, results into an accelerated exploration of the configurational space¹³. Such algorithms might employ a constant bias term (e.g. umbrella sampling¹⁴, hyperdynamics¹⁵, accelerated MD¹⁶, etc.) or a time-dependent one (e.g. local elevation¹⁷, conformational flooding¹⁸, metadynamics^{3,19,20}, adaptive biasing force^{21,22}, etc.). The crucial ingredient for almost all of the aforementioned algorithms is the *right choice* of the *collective variables*. The potential benefit and justification of enhanced sampling algorithms strongly depend on the quality of the collective variables as comprehensively elaborated in [23–25]. Physical intuition, experience gathered from previous simulation as well as quantitative methods for dimensionality reduction (e.g. by utilizing principal component analysis²⁶ (PCA)), potentially support the choice of reasonable collective variables. For complex materials-design problems and large-scale biochemical

processes, complexity exceeds our intuition and the question of “good” collective variables remains unanswered. Enhanced sampling methods employing inappropriate collective variables can be outperformed by brute force MD simulations²⁷. Thus, the identification of collective variables or reaction coordinates poses an important and difficult problem.

A systematic, robust, and general approach is needed for the discovery of lower-dimensional representations. Recent developments in dimensionality reduction methods provide a systematic strategy for discovering CVs¹³. For completeness, we give a brief overview of significant tools addressing CV discovery and dimensionality reduction in the context of molecular systems. An early study²⁸ found a steep decay in the eigenvalues of peptide trajectories indicating the existence of a low-dimensional representation that is capable of capturing essential physics. This study is based on PCA^{26,29} which identifies a linear coordinate transformation for best capturing the variance. However, the linear coordinate transformations employed merely describe local fluctuations in the context of peptide trajectories. Multidimensional scaling (MDS)^{30,31} identifies a lower-dimensional embedding such that pairwise distances (e.g. root-mean-square deviation (RMSD)) between atomistic configurations are best preserved. Sketch-map³² focuses on preserving “middle” ranged RMSD between trajectory pairs. Middle ranged RMSD pairs are the most relevant for observing pertinent behavior of the system³². Isometric feature map or ISOMAP³³ follows a similar idea of preserving geodesic distances. The aforementioned methods require dense sampling and encounter problems if the training data is non-uniformly distributed^{34–36}. Furthermore, we note that those methods involve a mapping from the atomistic configurations to the CVs whereas predictive tasks require a generative mapping from the CVs to the atomistic configuration.

Another group of non-linear dimensionality reductions methods follow the idea of approximating the eigenfunctions of the backward Fokker-Plank operator³⁷ by identifying eigenvalues and eigenvectors of transition kernels. The employed kernels resemble transition probabilities between configurations that we aim to preserve. For example, the diffusion map^{38–40} retains the diffusion distance by the identified coordinates for dynamic⁴¹ and stochastic systems⁴². A variation of diffusion maps exploits locally scaled diffusion maps (LS-DMap)³⁴ which calculate the transition probabilities between two configurations, utilizing the RMSD instead of an Euclidean distance. An additional local scale parameter, indicating the distance around a specific configuration presumably could be well approximated by a

low-dimensional hyperplane tangent. LSDMap is applied in [43] and enhances the exploration of the configurational space as shown in [44]. More recent approaches to collective variable discovery work under a common variational approach for conformation dynamics (VAC)⁴⁵ and employ a combination of basis functions for defining the eigenfunctions to the backward Fokker-Planck operator. One approach under VAC was developed in the context of metadynamics¹⁹ combining ideas from time-lagged independent component analysis and well-tempered metadynamics⁴⁶. Further developments have focused on alternate distance metrics, relying either on a kinetic distance which measures how slowly configurations interconvert⁴⁷, or on the commute distance⁴⁸ which provides an extension (arising by integration) of the former.

Several methods rely on the estimation of the eigenvectors of transitions matrices which is an expensive task in terms of computational cost. The need for “large” training datasets (e.g. 10,000 datapoints are required for robustness of the results¹³) limits the applicability of these methods to less complex systems. We refer to [49] for a critical review and comparison of the various methodologies mentioned before.

In this work, we propose a data-driven reformulation of the identification of CVs under the paradigm of probabilistic (Bayesian) inference. The methodology implies a generative model, considering CVs as lower-dimensional (latent) generators⁵⁰ of the full atomistic trajectory. The focus furthermore is on problems where limited atomistic training data are available that prohibit the accurate calculation of statistics for quantities of interest. Our approach is to compute an approximation of the underlying probabilistic distribution of the data. We then use this approximate distribution in a generative manner to perform accurate Monte Carlo estimation of the quantities of interest. To account for the limited information provided by the small size training dataset, epistemic uncertainties on quantities of interest are also computed within the Bayesian paradigm.

In the context of coarse-graining atomistic systems, latent variable models have been introduced in [51 and 52]. We optimize a flexible non-linear mapping between CVs and atomistic coordinates which implicitly specifies the meaning of the CVs. The identified CVs provide physical/chemical insight into the characteristics of the considered system. In the proposed model, the posterior distribution of the CVs given an atomistic data point is computed. This posterior provides a pre-image of the atomistic representation in the lower-dimensional latent space. We utilize recent developments in machine learning and

deep Bayesian modeling (Auto-Encoding Variational Bayes [53 and 54]). While typically deep learning models rely on huge amounts on data, we demonstrate the robustness of the proposed methodology considering only small and highly-variable datasets (e.g. 50 data points compared to 10,000 as required in the aforementioned methods). The proposed strategy requires significantly less data as compared to MDS^{30,31}, ISOMAP³³, and diffusion map^{38–40} and simultaneously enables the quantification of uncertainties arising from limited data. We also discuss how additional datapoints can be readily incorporated by efficiently updating the previously trained model without the need of solving a new eigenvalue problem.

Apart from the possibility of utilizing the discovered CVs for dimensionality reduction and enhanced sampling, we exploit them for *predictive* purposes i.e. for generating new atomistic configurations and estimating macroscopic observables. One could draw similarities between the identification of CVs and the problem of identifying a good coarse-grained representation^{51,55–65}. In addition, rather than solely obtaining point estimates of observables, the Bayesian framework adopted provides whole distributions which capture the epistemic uncertainty. This uncertainty propagates in the form of error bars around the predicted observables.

Several recent publications focus on similar problems^{66–68}. The present work clearly differs from [68] where the data is provided in a pre-processed form of sine and cosine backbone dihedral angles, i.e. not the full-atom configurations. The approach in [67] utilizes a pre-reduced representation of heavy atom positions as training data. While this is valid, it necessitates physical insight which might be not available for unexplored complex chemical compounds. In contrast, we rely on training data represented as Cartesian coordinates comprising all atoms of the considered system. We do not consider any physically- or chemically-motivated transformation nor do we perform any preprocessing of the dataset. Instead, we reveal, given the dimensionality of the CVs, important characteristics (i.e. dihedral angles, heavy atom positions) or less relevant fluctuations (noise) from the full atomistic picture. This work is also distinguished by following throughout a formalism based on Bayesian Learning. Instead of adopting or designing optimization objectives or loss functions, we consistently work within a Bayesian framework where the objective naturally arises. Furthermore, this readily allows us to make use of sparsity-inducing priors which reveal parsimonious features. The work of [8] is based on auto-associative artificial neural networks (autoencoders) which allow the encoding and reconstruction of atomistic configurations given an input da-

tum. Ref. [8] relies on reduced Cartesian coordinates in the form of backbone atoms which induces information loss. In addition, the focus in [8] is on CV discovery and enhanced sampling whereas we focus on CV discovery and obtaining a predictive model accounting for epistemic uncertainty.

The structure of the rest of the paper is as follows. Section II presents the basic model components, the use of Variational Autoencoders (VAEs,⁵³) in the CV discovery, and provides details on the learning algorithms employed. Numerical evidence of the capabilities of the proposed framework is provided in Section III. We identify CVs for alanine dipeptide and show the correlation between the discovered CVs and the intuitively-known ones i.e. the dihedral angles. We furthermore assess the predictive quality of the discovered CVs and estimate observables augmented by credible intervals. We show the dependence of credible intervals on the amount of training data. We also present the results of a similar analysis for a more complex and higher-dimensional molecule i.e. the ALA-15 peptide. Finally, Section IV summarizes the key findings of this paper and provides a brief discussion on potential extensions.

II. METHODS

After introducing the main notational convention in the context of equilibrium statistical mechanics, this section is devoted to the key concepts of generative latent variable models and variational inference⁶⁹ with emphasis on the identification of collective variables in atomistic systems.

A. Equilibrium statistical mechanics

We denote the coordinates of atoms of a molecular ensemble as $\mathbf{x} \in \mathcal{M}_f \subset \mathbb{R}^{n_f}$, with $n_f = \dim(\mathbf{x})$. The coordinates \mathbf{x} follow the Boltzmann-Gibbs density,

$$p_{target}(\mathbf{x}) = \frac{1}{Z(\beta)} e^{-\beta U(\mathbf{x})}, \quad (1)$$

with the interatomic potential $U(\mathbf{x})$, $\beta = \frac{1}{k_b T}$ where k_b is the Boltzmann constant and T the temperature. The normalization constant is given as $Z(\beta) = \int_{\mathcal{M}_f} \exp\{-\beta U(\mathbf{x})\} d\mathbf{x}$. MD simulations⁷⁰, or Monte-Carlo-based methods⁷¹ allow us to obtain samples from the

distribution defined in Eq. (1). In the following, we assume that a dataset, $\mathbf{X} = \{\mathbf{x}^{(i)}\}_{i=1}^N$, has been collected, where $\mathbf{x}^{(i)} \sim p_{\text{target}}(\mathbf{x})$. N denotes the amount of data points considered. The dataset \mathbf{X} will be used for training the generative model to be introduced in the sequel. The underlying assumption in this work is that the size of the available training dataset \mathbf{X} is small and not sufficient to compute directly statistics of observables. Our focus is thus on deriving an approximation to the distribution in Eq. (1) from which, in a computationally inexpensive manner, one can sample sufficient realizations of \mathbf{x} to allow probabilistic estimates of observables.

As elaborated in [13], the collection of a dataset \mathbf{X} that sufficiently captures the configurational space constitutes a difficult problem of its own. Hampered by free-energy barriers, a MD simulation is not guaranteed to visit all conformations of an atomistic system within a finite simulation time. The discovery of CVs can facilitate the development of enhanced sampling methods^{3,19,23} to address the efficient exploration of the configurational space.

This study considers systems in equilibrium for a given constant temperature T and consequently constant β . Optimally, the CVs discovered should be suitable for a range of temperatures²⁵. Section IV provides extensions of the model to address this issue.

B. Probabilistic generative models

Deep learning⁷² integrated with probabilistic modeling⁷³ has impacted many research areas⁷⁴. In this paper, we emphasize a subset of these models referred to as *probabilistic generative models*^{50,75}.

The objective is to identify CVs associated with relevant configurational changes of the system of interest. We consider CVs as hidden (low-dimensional) generators, giving rise to the observed atomistic configurations \mathbf{x} ⁷⁶. Extending the variable space of atomistic coordinates \mathbf{x} by latent CVs denoted as $\mathbf{z} \in \mathcal{M}_{\text{CV}} \subset \mathbb{R}^{n_{\text{CV}}}$, with $n_{\text{CV}} = \dim(\mathbf{z})$ and $\dim(\mathbf{z}) \ll \dim(\mathbf{x})$, allows us to define a joint distribution over the observed data \mathbf{x} and latent CVs^{50,77} $p(\mathbf{x}, \mathbf{z})$. The joint distribution $p(\mathbf{x}, \mathbf{z})$ is written as,

$$p(\mathbf{x}, \mathbf{z}) = p(\mathbf{x}|\mathbf{z}) p(\mathbf{z}). \quad (2)$$

In Eq. (2), $p(\mathbf{z})$ prescribes the distribution of the CVs and $p(\mathbf{x}|\mathbf{z})$ represents the conditional probability of the full atomistic coordinates \mathbf{x} given their latent representation \mathbf{z} . The prob-

abilistic connection between the latent CVs \mathbf{z} and the atomistic representation \mathbf{x} implicitly defines the meaning of the CVs.

Marginalizing the joint representation of Eq. (2) with respect the CVs leads to $\bar{p}(\mathbf{x})$,

$$\bar{p}(\mathbf{x}) = \int_{\mathcal{M}_{\text{CV}}} p(\mathbf{x}, \mathbf{z}) d\mathbf{z} = \int_{\mathcal{M}_{\text{CV}}} p(\mathbf{x}|\mathbf{z}) p(\mathbf{z}) d\mathbf{z}. \quad (3)$$

Eq. (3) provides a generative model for the atomistic configurations \mathbf{x} and will be utilized as an efficient estimator for observables of the atomistic system. Standard autoencoders in the context of CV discovery⁸ do not yield a probabilistic, predictive model which is the focus of this work. With appropriate selection of $p(\mathbf{z})$ and $p(\mathbf{x}|\mathbf{z})$, the resulting predictive distribution $\bar{p}(\mathbf{x})$ should resemble the atomistic reference $p(\mathbf{x})$ in Eq. (1). In order to quantify the closeness of the approximating distribution $\bar{p}(\mathbf{x})$ and the actual distribution $p(\mathbf{x})$, a distance measure is employed. The KL-divergence is one possibility out of the family of α -divergences^{78,7980} measuring the similarity between $p(\mathbf{x})$ and $\bar{p}(\mathbf{x})$. The non-negative valued KL-divergence is zero if and only if the two distributions coincide, which leads to the minimization objective with respect to $\bar{p}(\mathbf{x})$ of the following form:

$$\begin{aligned} D_{KL}(p_{\text{target}}(\mathbf{x})||p(\mathbf{x})) &= - \int_{\mathcal{M}_{\text{f}}} p_{\text{target}}(\mathbf{x}) \log \frac{p(\mathbf{x})}{p_{\text{target}}(\mathbf{x})} d\mathbf{x} \\ &= - \int_{\mathcal{M}_{\text{f}}} p_{\text{target}}(\mathbf{x}) \log p(\mathbf{x}) d\mathbf{x} \\ &\quad + \int_{\mathcal{M}_{\text{f}}} p_{\text{target}}(\mathbf{x}) \log p_{\text{target}}(\mathbf{x}) d\mathbf{x}. \end{aligned} \quad (4)$$

We introduce a parametrization $\boldsymbol{\theta}$ of the approximating distribution as $\bar{p}(\mathbf{x}|\boldsymbol{\theta}) = \int_{\mathcal{M}_{\text{CV}}} p_{\boldsymbol{\theta}}(\mathbf{x}|\mathbf{z}) p_{\boldsymbol{\theta}}(\mathbf{z}) d\mathbf{z}$. Instead of minimizing the KL-divergence with respect to $p(\mathbf{x})$, one can optimize the objective with respect to the parameters $\boldsymbol{\theta}$. We note that the minimization of Eq. (4) is equivalent to maximizing the expression $\int_{\mathcal{M}_{\text{f}}} p_{\text{target}}(\mathbf{x}) \log p(\mathbf{x}) d\mathbf{x}$. If we consider a data-driven approach where $p(\mathbf{x})$ is approximated by a finite-sized dataset \mathbf{X} , we can write the problem as the maximization of the the log-likelihood $\log p_{\boldsymbol{\theta}}(\mathbf{x}^{(i)}, \dots, \mathbf{x}^{(N)})$:

$$\begin{aligned} \log p(\mathbf{X}|\boldsymbol{\theta}) &= \sum_{i=1}^N \log p(\mathbf{x}^{(i)}|\boldsymbol{\theta}) \\ &= \sum_{i=1}^N \log \left(\int_{\mathcal{M}_{\text{CV}}} p_{\boldsymbol{\theta}}(\mathbf{x}^{(i)}|\mathbf{z}^{(i)}) p_{\boldsymbol{\theta}}(\mathbf{z}^{(i)}) d\mathbf{z}^{(i)} \right). \end{aligned} \quad (5)$$

Maximizing Eq. (5) with respect to the model parameters $\boldsymbol{\theta}$ results into the maximum likelihood estimate $\boldsymbol{\theta}_{\text{MLE}}$. By introducing a prior $p(\boldsymbol{\theta})$ on the parameters, one can augment

this optimization problem to compute the Maximum a Posteriori (MAP) estimate^{81–83} as follows:

$$\arg \max_{\boldsymbol{\theta}} \{ \log p(\mathbf{X}|\boldsymbol{\theta}) + \log p(\boldsymbol{\theta}) \}. \quad (6)$$

The full posterior could also be obtained by applying Bayes' rule,

$$p(\boldsymbol{\theta}|\mathbf{X}) = \frac{p(\mathbf{X}|\boldsymbol{\theta})p(\boldsymbol{\theta})}{p(\mathbf{X})}. \quad (7)$$

Quantifying uncertainties in $\boldsymbol{\theta}$ enables us to capture the epistemic uncertainty introduced from the limited training data. The discovery of CVs through Bayesian inference is elaborated in the sequel.

C. Inference and learning

This section focuses on the details of inference and parameter learning for the generative model introduced in Eq. (3). Both tasks are facilitated by approximate variational inference⁸⁴ and stochastic backpropagation^{54,85,86} which we discuss next.

Direct optimization of the marginal likelihood $p(\mathbf{x}|\boldsymbol{\theta})$ requires the evaluation of $p(\mathbf{x}|\boldsymbol{\theta}) = \int_{\mathcal{M}_{\text{CV}}} p_{\boldsymbol{\theta}}(\mathbf{x}|\mathbf{z})p_{\boldsymbol{\theta}}(\mathbf{z}) d\mathbf{z}$ which constitutes an intractable integration over \mathcal{M}_{CV} . The posterior $p_{\boldsymbol{\theta}}(\mathbf{z}|\mathbf{x}) = p_{\boldsymbol{\theta}}(\mathbf{x}|\mathbf{z})p_{\boldsymbol{\theta}}(\mathbf{z})/p(\mathbf{x}|\boldsymbol{\theta})$ is also computationally intractable. Therefore, the direct application of Expectation-Maximization^{87,88} is not applicable. To that end, we reformulate the log-likelihood for the dataset $\mathbf{X} = \{\mathbf{x}^{(i)}\}_{i=1}^N$ by introducing auxiliary densities $q_{\phi}(\mathbf{z}^{(i)}|\mathbf{x}^{(i)})$ parametrized by ϕ . The meaning of $q_{\phi}(\mathbf{z}^{(i)}|\mathbf{x}^{(i)})$ will be specified later in the text. The log-likelihood follows,

$$\begin{aligned} \log p(\mathbf{X}|\boldsymbol{\theta}) &= \sum_{i=1}^N \log \bar{p}(\mathbf{x}^{(i)}|\boldsymbol{\theta}) \\ &= \sum_{i=1}^N \log \int_{\mathcal{M}_{\text{CV}}} p_{\boldsymbol{\theta}}(\mathbf{x}^{(i)}|\mathbf{z}^{(i)})p_{\boldsymbol{\theta}}(\mathbf{z}^{(i)}) d\mathbf{z}^{(i)} \\ &= \sum_{i=1}^N \log \int_{\mathcal{M}_{\text{CV}}} q_{\phi}(\mathbf{z}^{(i)}|\mathbf{x}^{(i)}) \frac{p_{\boldsymbol{\theta}}(\mathbf{x}^{(i)}|\mathbf{z}^{(i)})p_{\boldsymbol{\theta}}(\mathbf{z}^{(i)})}{q_{\phi}(\mathbf{z}^{(i)}|\mathbf{x}^{(i)})} d\mathbf{z}^{(i)} \\ &\geq \sum_{i=1}^N \underbrace{\int_{\mathcal{M}_{\text{CV}}} q_{\phi}(\mathbf{z}^{(i)}|\mathbf{x}^{(i)}) \log \frac{p_{\boldsymbol{\theta}}(\mathbf{x}^{(i)}|\mathbf{z}^{(i)})p_{\boldsymbol{\theta}}(\mathbf{z}^{(i)})}{q_{\phi}(\mathbf{z}^{(i)}|\mathbf{x}^{(i)})} d\mathbf{z}^{(i)}}_{\mathcal{L}(\boldsymbol{\theta}, \phi; \mathbf{x}^{(i)})}, \end{aligned} \quad (8)$$

where in the last step we have made use of Jensen’s inequality. Note that for each data point $\mathbf{x}^{(i)}$, one latent CV $\mathbf{z}^{(i)}$ is assigned. The lower-bound of the marginal log-likelihood is:

$$\mathcal{L}(\boldsymbol{\theta}, \boldsymbol{\phi}; \mathbf{X}) = \sum_{i=1}^N \mathcal{L}(\boldsymbol{\theta}, \boldsymbol{\phi}; \mathbf{x}^{(i)}). \quad (9)$$

and implicitly depends on $\boldsymbol{\phi}$ through the parametrization of $q_{\boldsymbol{\phi}}(\mathbf{z}|\mathbf{x})$. For each data point $\mathbf{x}^{(i)}$ and from the definition of $\mathcal{L}(\boldsymbol{\theta}, \boldsymbol{\phi}; \mathbf{x}^{(i)})$, one can rewrite the log-likelihoods $\log p(\mathbf{x}^{(i)}|\boldsymbol{\theta})$ as,

$$\log p(\mathbf{x}^{(i)}|\boldsymbol{\theta}) = D_{KL}(q_{\boldsymbol{\phi}}(\mathbf{z}^{(i)}|\mathbf{x}^{(i)})||p_{\boldsymbol{\theta}}(\mathbf{z}^{(i)}|\mathbf{x}^{(i)})) + \mathcal{L}(\boldsymbol{\theta}, \boldsymbol{\phi}; \mathbf{x}^{(i)}) \geq \mathcal{L}(\boldsymbol{\theta}, \boldsymbol{\phi}; \mathbf{x}^{(i)}). \quad (10)$$

Since the KL-divergence is always non-negative, the inequalities in Eq. (8) and Eq. (10) become equalities if and only if $q_{\boldsymbol{\phi}}(\mathbf{z}^{(i)}|\mathbf{x}^{(i)}) = p_{\boldsymbol{\theta}}(\mathbf{z}^{(i)}|\mathbf{x}^{(i)})$ as in this case $D_{KL}(q_{\boldsymbol{\phi}}(\mathbf{z}|\mathbf{x}^{(i)})||p_{\boldsymbol{\theta}}(\mathbf{z}^{(i)}|\mathbf{x}^{(i)})) = 0$. Thus $q_{\boldsymbol{\phi}}(\mathbf{z}^{(i)}|\mathbf{x}^{(i)})$ can be thought of as an approximation of the posterior. If the lower-bound gets tight, $q_{\boldsymbol{\phi}}(\mathbf{z}^{(i)}|\mathbf{x}^{(i)})$ equals the exact posterior $p_{\boldsymbol{\theta}}(\mathbf{z}|\mathbf{x}^{(i)})$.

Equation (8) can also be written as follows,

$$\begin{aligned} \mathcal{L}(\boldsymbol{\theta}, \boldsymbol{\phi}; \mathbf{X}) &= \sum_{i=1}^N \mathbb{E}_{q_{\boldsymbol{\phi}}(\mathbf{z}^{(i)}|\mathbf{x}^{(i)})} [-\log q_{\boldsymbol{\phi}}(\mathbf{z}^{(i)}|\mathbf{x}^{(i)}) + \log p_{\boldsymbol{\theta}}(\mathbf{x}^{(i)}, \mathbf{z}^{(i)})] \\ &= - \sum_{i=1}^N D_{KL}(q_{\boldsymbol{\phi}}(\mathbf{z}^{(i)}|\mathbf{x}^{(i)})||p_{\boldsymbol{\theta}}(\mathbf{z}^{(i)})) + \sum_{i=1}^N \mathbb{E}_{q_{\boldsymbol{\phi}}(\mathbf{z}^{(i)}|\mathbf{x}^{(i)})} [\log p_{\boldsymbol{\theta}}(\mathbf{x}^{(i)}|\mathbf{z}^{(i)})]. \end{aligned} \quad (11)$$

It is clear from Eq. (11) that the lower-bound balances the optimization of the following two objectives⁵³:

1. Minimizing $\sum_{i=1}^N D_{KL}(q_{\boldsymbol{\phi}}(\mathbf{z}^{(i)}|\mathbf{x}^{(i)})||p_{\boldsymbol{\theta}}(\mathbf{z}))$ regularizes the posterior $q_{\boldsymbol{\phi}}(\mathbf{z}^{(i)}|\mathbf{x}^{(i)})$ such that *on average* over all data points $\mathbf{x}^{(i)}$ resembles $p_{\boldsymbol{\theta}}(\mathbf{z})$. We expect highly probable atomistic configurations $\mathbf{x}^{(i)}$ to be encoded to CVs $\mathbf{z}^{(i)}$ located in regions with high probability mass in $p_{\boldsymbol{\theta}}(\mathbf{z})$. The posterior $q_{\boldsymbol{\phi}}(\mathbf{z}^{(i)}|\mathbf{x}^{(i)})$ accounts for this and supports findings presented in [67].
2. $\mathbb{E}_{q_{\boldsymbol{\phi}}(\mathbf{z}^{(i)}|\mathbf{x}^{(i)})} [\log p_{\boldsymbol{\theta}}(\mathbf{x}^{(i)}|\mathbf{z}^{(i)})]$ is the negative expected reconstruction error employing the encoded pre-image of the data $\mathbf{x}^{(i)}$ in the latent CV space. For example assuming $p_{\boldsymbol{\theta}}(\mathbf{x}^{(i)}|\mathbf{z}^{(i)})$ to be a Gaussian with mean $\boldsymbol{\mu}(\mathbf{z}^{(i)})$ and variance $\boldsymbol{\sigma}^2$, one can rewrite

$\mathbb{E}_{q_\phi(\mathbf{z}^{(i)}|\mathbf{x}^{(i)})}[\log p_\theta(\mathbf{x}^{(i)}|\mathbf{z}^{(i)})]$ as,

$$\begin{aligned}\mathbb{E}_{q_\phi(\mathbf{z}^{(i)}|\mathbf{x}^{(i)})}[\log p_\theta(\mathbf{x}^{(i)}|\mathbf{z}^{(i)})] &= \mathbb{E}_{q_\phi(\mathbf{z}^{(i)}|\mathbf{x}^{(i)})} \left[-\frac{1}{2} \frac{(\mathbf{x}^{(i)} - \boldsymbol{\mu}(\mathbf{z}^{(i)}))^2}{\boldsymbol{\sigma}^2} \right] + \text{const.} \\ &\propto -\mathbb{E}_{q_\phi(\mathbf{z}^{(i)}|\mathbf{x}^{(i)})} \left[(\mathbf{x}^{(i)} - \boldsymbol{\mu}(\mathbf{z}^{(i)}))^2 \right] \\ &= -\int_{\mathcal{M}_{\text{CV}}} q_\phi(\mathbf{z}^{(i)}|\mathbf{x}^{(i)}) (\mathbf{x}^{(i)} - \boldsymbol{\mu}(\mathbf{z}^{(i)}))^2 d\mathbf{z}^{(i)}. \quad (12)\end{aligned}$$

The second line of Eq. (12) is the negative expected error of reconstructing the atomistic configuration $\mathbf{x}^{(i)}$ through the decoder $p_\theta(\mathbf{x}^{(i)}|\mathbf{z}^{(i)})$. The expectation (see last line in Eq. (12)) is evaluated with respect to $q_\phi(\mathbf{z}^{(i)}|\mathbf{x}^{(i)})$ and therefore with respect to all CVs $\mathbf{z}^{(i)}$ probabilistically assigned to $\mathbf{x}^{(i)}$.

The approximate posterior q_ϕ serves as a recognition model and is called the encoder⁵³. Atomistic configurations \mathbf{x} can be mapped via $q_\phi(\mathbf{z}|\mathbf{x})$ to their lower-dimensional representation \mathbf{z} in the CV space. Hence, each \mathbf{z} could be interpreted as a (latent) *encoding* of an \mathbf{x} . Its counterpart, the decoder $p_\theta(\mathbf{x}|\mathbf{z})$, probabilistically maps CVs \mathbf{z} to atomistic configurations \mathbf{x} . As it will be demonstrated in the sequel, \mathbf{z} sampled from $p_\theta(\mathbf{z})$ will be used to reconstruct atomistic configurations via $p_\theta(\mathbf{x}|\mathbf{z})$. Note that we do not require any physicochemical meaning assigned to the latent CVs that are identified implicitly during the training process.

The (approximate) inference task of $q_\phi(\mathbf{z}|\mathbf{x})$ has been re-formulated as an optimization problem with respect to the parameters ϕ . These will be updated in combination with the parameters θ as described in the following. At this point, we emphasize that the lower-bound $\mathcal{L}(\theta, \phi; \mathbf{x}^{(i)})$ on the marginal log-likelihood (unobserved CVs are marginalized out) of Eq. (11) has been used as a negative “loss” function in non-Bayesian applications of autoencoders in the context of atomistic simulations as in^{66,68}.

In order to carry out the optimization $\mathcal{L}(\phi, \theta; \mathbf{X})$ with respect to $\{\phi, \theta\}$, first-order derivatives are needed of terms involving expectations w.r.t q_ϕ as it can be seen in Eq. (11). Consider in general a function $f(\mathbf{z})$ and the corresponding expectation $\mathbb{E}_{q_\phi(\mathbf{z}|\mathbf{x})}[f(\mathbf{z})]$. Its gradient with respect to ϕ can be expressed as

$$\nabla_\phi \mathbb{E}_{q_\phi(\mathbf{z}|\mathbf{x})}[f(\mathbf{z})] = \mathbb{E}_{q_\phi(\mathbf{z}|\mathbf{x})} [f(\mathbf{z}) \nabla_{q_\phi(\mathbf{z}|\mathbf{x})} \log q_\phi(\mathbf{z}|\mathbf{x})], \quad (13)$$

and the expectation $\mathbb{E}_{q_\phi(\mathbf{z}|\mathbf{x})}[\cdot]$ on the right hand-side can be approximated via a Monte-Carlo (MC) estimate using samples of \mathbf{z} drawn from $q_\phi(\mathbf{z}|\mathbf{x})$. It is however known⁸⁵ that

the variance of such estimators can be very high which adversely affects the optimization process. The high variance of the estimator in Eq. (13) can be addressed with the so-called reparametrization trick^{53,54}. It is based on expressing \mathbf{z} by auxiliary random variables $\boldsymbol{\epsilon}$ and a differentiable transformation $g_\phi(\boldsymbol{\epsilon}, \mathbf{x})$ as

$$\mathbf{z} = g_\phi(\boldsymbol{\epsilon}, \mathbf{x}) \text{ with } \boldsymbol{\epsilon} \sim p(\boldsymbol{\epsilon}). \quad (14)$$

The density $p(\boldsymbol{\epsilon})$ as well as the function g_ϕ are selected such that the resulting distribution of \mathbf{z} is $q_\phi(\mathbf{z}|\mathbf{x})$. Several such transformations have been documented for typical densities (e.g. Gaussians)⁸⁹. The change of variables leads to the following expression for the gradient,

$$\nabla_\phi \mathbb{E}_{q_\phi(\mathbf{z}|\mathbf{x})}[f(\mathbf{z})] = \mathbb{E}_{p(\boldsymbol{\epsilon})}[\nabla_\phi f(g_\phi(\boldsymbol{\epsilon}, \mathbf{x}))] = \mathbb{E}_{p(\boldsymbol{\epsilon})} \left[\frac{\partial f(g_\phi(\boldsymbol{\epsilon}, \mathbf{x}))}{\partial \mathbf{z}} \frac{\partial g_\phi(\boldsymbol{\epsilon}, \mathbf{x})}{\partial \boldsymbol{\phi}} \right], \quad (15)$$

which can in turn be calculated by Monte Carlo using samples of $\boldsymbol{\epsilon}$ drawn from $p(\boldsymbol{\epsilon})$. Based on this, we define the following modified estimator for the lower-bound⁵³,

$$\begin{aligned} \tilde{\mathcal{L}}(\phi, \boldsymbol{\theta}; \mathbf{x}^{(i)}) &= -D_{KL}(q_\phi(\mathbf{z}^{(i)}|\mathbf{x}^{(i)})||p_\theta(\mathbf{z})) + \frac{1}{L} \sum_{l=1}^L \log p_\theta(\mathbf{x}^{(i)}|\mathbf{z}^{(i,l)}) \\ \text{with } \mathbf{z}^{(i,l)} &= g_\phi(\boldsymbol{\epsilon}^{(l)}, \mathbf{x}^{(i)}) \text{ and } \boldsymbol{\epsilon}^{(l)} \sim p(\boldsymbol{\epsilon}). \end{aligned} \quad (16)$$

Note that for the particular forms of $q_\phi(\mathbf{z}^{(i)}|\mathbf{x}^{(i)})$ and $p_\theta(\mathbf{z})$ selected in Section III A 2, $D_{KL}(q_\phi(\mathbf{z}^{(i)}|\mathbf{x}^{(i)})||p_\theta(\mathbf{z}))$ becomes an analytically tractable expression. In order to increase the computational efficiency, we work with a sub-sampled minibatch \mathbf{X}^M comprising of M datapoints from \mathbf{X} , with $M < N$. This leads to $\lfloor M/N \rfloor$ minibatches, each uniformly sampled from \mathbf{X} . The corresponding estimator of the lower-bound on the marginal log-likelihood is then given as,

$$\mathcal{L}(\phi, \boldsymbol{\theta}; \mathbf{X}) \simeq \tilde{\mathcal{L}}^M(\boldsymbol{\theta}, \phi; \mathbf{X}^M) = \frac{N}{M} \sum_{i=1}^M \tilde{\mathcal{L}}(\boldsymbol{\theta}, \phi; \mathbf{x}^{(i)}), \quad (17)$$

with $\tilde{\mathcal{L}}(\boldsymbol{\theta}, \phi; \mathbf{x}^{(i)})$ computed in Eq. (16). The factor N/M in Eq. (17) rescales $\sum_{i=1}^M \tilde{\mathcal{L}}(\boldsymbol{\theta}, \phi; \mathbf{x}^{(i)})$ such that the lower-bound $\tilde{\mathcal{L}}^M(\boldsymbol{\theta}, \phi; \mathbf{X}^M)$ computed by $M < N$ datapoints approximates the actual lower-bound $\mathcal{L}(\phi, \boldsymbol{\theta}; \mathbf{X})$ computed with N datapoints⁵³. However, note that using a subset of the datapoints unavoidably increases the variance in the stochastic gradient estimator Eq. (16). Strategies compensating this increase are presented in [90]. The overall procedure is summarized in Algorithm 1.

We finally note that new data can be readily incorporated by augmenting accordingly the objective and initializing the algorithm with the optimal parameter values found up to that point. In fact this strategy was adopted in the results presented in the Section III and led to significant efficiency gains. One can envision a running all-atom simulation which sequentially generates new training data that are automatically and quickly ingested by the proposed coarse-grained model which is in turn used to produce predictive estimates as will be described in the sequel. In contrast, other dimensionality reduction methods based on the solution of an eigenvalue problem are required to solve the system anew for the whole dataset when new data is presented.

Algorithm 1 Stochastic Variational Inference algorithm.

$\{\theta, \phi\} \leftarrow$ Initialize parameters.

repeat

$\mathbf{X}^M \leftarrow$ Random minibatch of M datapoints drawn from dataset \mathbf{X} .

$\epsilon \leftarrow$ Random sample(s) from noise distribution $p(\epsilon)$.

$\mathbf{g} \leftarrow \nabla_{\phi, \theta} \mathcal{L}^M(\phi, \theta; \mathbf{X}^M, \epsilon)$ Calculate gradients with the estimator in Eq. (17).

$\{\phi, \theta\} \leftarrow$ Update parameters with gradient \mathbf{g} (e.g. with Adam, see [91]).

until Convergence of $\{\theta, \phi\}$.

return $\{\theta, \phi\}$.

D. Predicting atomistic configurations - Leveraging the exact likelihood

After training the model as described in the previous Section II C, we are interested in obtaining the predictive distribution $\bar{p}(\mathbf{x}|\theta) = \int_{\mathcal{M}_{\text{CV}}} p_{\theta}(\mathbf{x}|\mathbf{z}) p_{\theta}(\mathbf{z}) d\mathbf{z}$ (see Eq. (3)) which poses a demanding computational task. One approach for predicting configurations \mathbf{x} distributed according to $\bar{p}(\mathbf{x}|\theta)$ is ancestral sampling. Firstly, one can generate a sample \mathbf{z}^l from $p_{\theta}(\mathbf{z})$ and secondly sample $\mathbf{x}^{(k,l)} \sim p_{\theta}(\mathbf{x}|\mathbf{z}^l)$. The variance of such estimators significantly increases with increasing $\dim(\mathbf{z})$. Ancestral sampling does not account for training the model by employing an *approximate* posterior $q_{\phi}(\mathbf{z}|\mathbf{x})$ instead of the actual posterior $p_{\theta}(\mathbf{z}|\mathbf{x})$. The *Metropolis-within-Gibbs* sampling scheme⁹² corrects and accounts for grounding the optimization of the objective in Eq. (11) on an imperfect variational approximation. This approach builds upon findings in [54] and proposes that generated samples $\bar{\mathbf{x}}$ follow a Markov chain $(\mathbf{z}_t, \bar{\mathbf{x}}_t)$ for steps $t \geq 1$. Ref. [92] proposes employing the following Metropo-

lis^{93,94} update criterion ρ_t reflecting a ratio of importance ratios,

$$\rho_t = \frac{\frac{p_{\theta}(\bar{\mathbf{x}}_{t-1}|\tilde{\mathbf{z}}_t) p_{\theta}(\tilde{\mathbf{z}}_t)}{p_{\theta}(\bar{\mathbf{x}}_{t-1}|\mathbf{z}_{t-1}) p_{\theta}(\mathbf{z}_{t-1})}}{\frac{q_{\phi}(\tilde{\mathbf{z}}_t|\bar{\mathbf{x}}_{t-1})}{q_{\phi}(\mathbf{z}_{t-1}|\bar{\mathbf{x}}_{t-1})}}. \quad (18)$$

Eq. (18) corrects using the approximate posterior $q_{\phi}(\mathbf{z}|\mathbf{x})$. In case of identifying the exact posterior where $D_{KL}(q_{\phi}(\mathbf{z}|\mathbf{x})||p_{\theta}(\mathbf{z}|\mathbf{x})) = 0$, all proposals \mathbf{z}_t in Algorithm [2] get accepted with $\rho_t = 1$.

Algorithm 2 Metropolis-within-Gibbs sampler [92].

Input Trained model $p_{\theta}(\mathbf{x}|\mathbf{z})p_{\theta}(\mathbf{z})$ and approximate posterior $q_{\phi}(\mathbf{z}|\mathbf{x})$. Total steps T .

Initialize $(\mathbf{z}_0, \bar{\mathbf{x}}_0)$.

for $t = 1$ **to** T **do**

$\tilde{\mathbf{z}}_t \sim q_{\phi}(\mathbf{z}|\bar{\mathbf{x}}_{t-1})$ Draw proposal $\tilde{\mathbf{z}}_t$ from the approximate posterior $q_{\phi}(\mathbf{z}|\bar{\mathbf{x}}_{t-1})$.

$\rho_t = \frac{p_{\theta}(\bar{\mathbf{x}}_{t-1}|\tilde{\mathbf{z}}_t) p_{\theta}(\tilde{\mathbf{z}}_t)}{p_{\theta}(\bar{\mathbf{x}}_{t-1}|\mathbf{z}_{t-1}) p_{\theta}(\mathbf{z}_{t-1})} \frac{q_{\phi}(\mathbf{z}_{t-1}|\bar{\mathbf{x}}_{t-1})}{q_{\phi}(\tilde{\mathbf{z}}_t|\bar{\mathbf{x}}_{t-1})}$ Estimate the Metropolis acceptance ratio, correcting for the use of the approximate posterior distribution $q_{\phi}(\mathbf{z}|\mathbf{x})$.

$\mathbf{z}_t = \begin{cases} \tilde{\mathbf{z}}_t & \text{with probability } \rho_t \\ \mathbf{z}_{t-1} & \text{with probability } 1 - \rho_t. \end{cases}$

$\bar{\mathbf{x}}_t \sim p_{\theta}(\mathbf{x}|\mathbf{z}_t)$

end for

return $\bar{\mathbf{x}}_{1:T}$.

E. Prior specification

The recent work of [92] discusses the pitfalls of overly expressive, deep, latent variable models which can yield infinite likelihoods and ill-posed optimization problems⁹⁵. We address these issues by regularizing the log-likelihood with functional priors^{96,97}. The prior contribution is added as an additional component in the log-likelihood as indicated in Eq. (6). In addition to enhanced stability during training⁹², sparsity inducing priors alleviate the overparameterized nature of complex neural networks.

We adopt the Automatic Relevance Determination (ARD⁹⁸) model which consists of the following distributions:

$$p(\boldsymbol{\theta}|\boldsymbol{\tau}) \equiv \prod_k \mathcal{N}(\theta_k|0, \tau_k^{-1}), \quad \tau_k \sim \text{Gamma}(\tau_k|a_0, b_0). \quad (19)$$

Eq. (19) implies modeling each θ_k with an independent Gaussian distribution. The Gaussian distribution has zero-mean and an independent precision hyper-parameter τ_k , modeled with a (conjugate) Gamma density. The resulting prior $p(\theta_k)$ follows (by marginalizing the hyper-parameter τ_k) a heavy-tailed Student’s t -distribution. This distribution favors a priori sparse solutions with θ_k close to zero. In order to compute derivatives of the log-prior needed during learning of the parameters $\boldsymbol{\theta}$, we treat the τ_k ’s as latent variables in an inner-loop expectation-maximization scheme⁹⁹ which consists of the following steps:

- E-step - evaluate:

$$\langle \tau_k \rangle_{p(\tau_k|\theta_k)} = \frac{a_0 + \frac{1}{2}}{b_0 + \frac{\theta_k^2}{2}}. \quad (20)$$

- M-step - evaluate:

$$\frac{\partial \log p(\boldsymbol{\theta})}{\partial \theta_k} = - \langle \tau_k \rangle_{p(\tau_k|\theta_k)} \theta_k. \quad (21)$$

The second derivative of the log-prior with respect to $\boldsymbol{\theta}$ is obtained as:

$$\frac{\partial^2 \log p(\boldsymbol{\theta})}{\partial \theta_k \partial \theta_l} = \begin{cases} - \langle \tau_k \rangle_{p(\tau_k|\theta_k)}, & \text{if } k = l \\ 0, & \text{otherwise.} \end{cases} \quad (22)$$

The ARD choice of the hyper-parameters is $a_0 = b_0 = 1.0\text{e-}5$. In similar settings, e.g. coarse-graining of atomistic systems, the ARD prior identified the most salient features⁵¹, whereas in this context it improves stability and turns off unnecessary parameters for describing the training data.

F. Approximate Bayesian inference - Laplace’s approximation

Thus far, we have considered point estimates of the model parameters $\boldsymbol{\theta}$ (either MLE or MAP). A fully Bayesian treatment however requires the evaluation of the normalization constant of the exact posterior distribution $p(\boldsymbol{\theta}|\mathbf{X})$, which is computationally impractical. We advocate an approximation to the posterior of $\boldsymbol{\theta}$ that is based on Laplace’s method⁷⁶. The latter has been rediscovered as an efficient approximation for weight uncertainties in the context of neural networks in [100]. In Laplace’s approach, the exact posterior is approximated with a normal distribution with mean $\boldsymbol{\theta}_{\text{MAP}}$ and covariance the inverse of the negative Hessian of the log-posterior at $\boldsymbol{\theta}_{\text{MAP}}$. Here, we assume a Gaussian with diagonal

covariance matrix $\mathbf{S}_L = \text{diag}(\boldsymbol{\sigma}_L^2)$ as follows,

$$p(\boldsymbol{\theta}|\mathbf{X}) \approx \mathcal{N}(\boldsymbol{\mu}_L, \mathbf{S}_L = \text{diag}(\boldsymbol{\sigma}_L^2)), \quad (23)$$

with,

$$\boldsymbol{\mu}_L = \boldsymbol{\theta}_{\text{MAP}}, \quad (24)$$

and the diagonal entries of \mathbf{S}_L^{-1} ,

$$\sigma_{L,k}^{-2} = -\frac{\partial^2 \mathcal{L}(\phi, \boldsymbol{\theta}; \mathbf{X})}{\partial \theta_k^2} \big|_{\boldsymbol{\theta}_{\text{MAP}}, \phi_{\text{MAP}}} + \mathbb{E}_{p(\tau_k|\theta_k)}[\tau_k], \quad (25)$$

where the term $\mathbb{E}_{p(\tau_k|\theta_k)}[\tau_k]$ arises from the prior via Eq. (22). The quantities in Eq. (24) and Eq. (25) are obtained at the last iteration (upon convergence) of the Auto-Encoding Variational Bayes algorithm.

III. NUMERICAL ILLUSTRATIONS

The following section is devoted to the application of the proposed procedure for identifying collective variables of alanine dipeptide (ALA-2^{101,102}) as well as of a longer peptide i.e. ALA-15. We discuss the performance and robustness of the proposed methodology in the presence of a small amount of training data and emphasize the predictive capabilities of the model by the Ramachandran plot¹⁰³ and the radius of gyration. The predictions are augmented by error bars capturing epistemic uncertainty.

A. ALA-2

1. *Simulation of ALA-2*

Alanine dipeptide consists of 22 atoms leading to $\dim(\mathbf{x}) = 66$ in a Cartesian representation comprising the coordinates of *all* atoms which we will use later on as the model input. It is well-known that ALA-2 exhibits distinct conformations which are categorized depending on the dihedral angles (ϕ, ψ) (as indicated in Fig. 1(a)) of the atomistic configuration. We label the three characteristic modes as α , β -1, and β -2 in accordance with [104] (see Fig. 1(b)).

The procedure for generating the training data for ALA-2 is similar to that in [105]. The atoms of the alanine dipeptide interact via the AMBER ff96^{106–108} force field and we

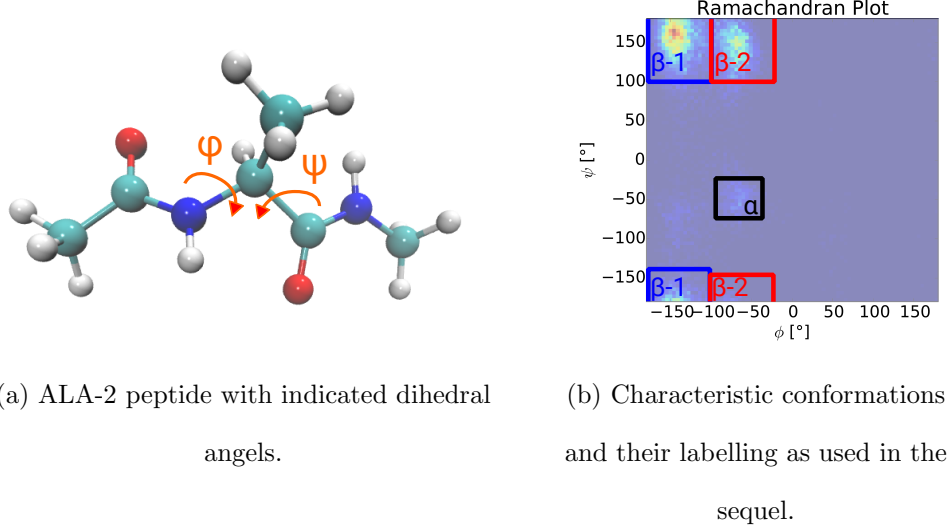


FIG. 1. Definition of the dihedral angles and the labelling of characteristic modes as utilized in this paper.

employ an implicit water model based on generalized Born/solvent accessible surface area model^{109,110}. However, we note that an explicit water model would better represent an experimental environment. We employ an Andersen thermostat and the simulations were carried out at constant temperature $T = 330$ K using Gromacs^{111–117}. The time step is taken as $\Delta t = 1$ fs with an equilibration phase of 50 ns. The training dataset consisted of snapshots taken every 10 ps after the equilibration phase. Rigid body motions have been removed from the dataset.

For demonstrating the encoding into the latent CV space of atomistic configurations not contained in the training dataset, we used a test dataset selected so that the dihedral angles (ϕ, ψ) had values belonging to all three modes i.e. α , β -1, and β -2 (defined in Fig. 1(b)).

2. Model specification

The model requires the specification of three components. Two components are needed to describe the generative model $p(\mathbf{x}|\boldsymbol{\theta})$: the probabilistic mapping $p_{\boldsymbol{\theta}}(\mathbf{x}|\mathbf{z})$ and the distribution of the CVs $p_{\boldsymbol{\theta}}(\mathbf{z})$. The third component is the approximate posterior $q_{\phi}(\mathbf{z}|\mathbf{x})$ as shown in Eq. (8).

Following [53], the distribution of the CVs is taken to be a standard Gaussian,

$$p_{\boldsymbol{\theta}}(\mathbf{z}) = p(\mathbf{z}) = \mathcal{N}(\mathbf{z}; \mathbf{0}, \mathbf{I}). \quad (26)$$

The simplicity in the distribution in Eq. (26) is compensated by a flexible mapping from \mathbf{z} to the atomistic coordinates \mathbf{x} . This probabilistic mapping (decoder) is given by a parametrized Gaussian as follows,

$$p_{\theta}(\mathbf{x}|\mathbf{z}) = \mathcal{N}(\mathbf{x}; \boldsymbol{\mu}_{\theta}(\mathbf{z}), \mathbf{S}_{\theta}) \quad (27)$$

where,

$$\boldsymbol{\mu}_{\theta}(\mathbf{z}) = f_{\theta}^{\mu}(\mathbf{z}), \quad (28)$$

is a non-linear mapping $\mathbf{z} \mapsto f_{\theta}^{\mu}(\mathbf{z})$ ($f_{\theta}^{\mu} : \mathbb{R}^{n_{cv}} \mapsto \mathbb{R}^{n_f}$) parametrized by an expressive multilayer perceptron^{118–120}. We consider a diagonal covariance matrix i.e. $\mathbf{S}_{\theta} = \text{diag}(\boldsymbol{\sigma}_{\theta}^2)^{92}$ where σ_{θ}^2 , are treated as model parameters and do not depend on the latent CVs \mathbf{z} . In order to ensure the non-negativity of $\sigma_{\theta,j}^2 > 0$ while performing unconstrained optimization, we operate instead on the $\log \sigma_{\theta,j}^2$.

The approximate posterior $q_{\phi}(\mathbf{z}^{(i)}|\mathbf{x}^{(i)})$ (encoder, approximating $p_{\theta}(\mathbf{z}^{(i)}|\mathbf{x}^{(i)})$) introduced in Eq. (8) is modeled by a Gaussian with flexible mean and variance represented by a neural network. For each pair of $\mathbf{x}^{(i)}, \mathbf{z}^{(i)}$ (for notational simplicity, we drop the index (i)):

$$q_{\phi}(\mathbf{z}|\mathbf{x}) = \mathcal{N}(\mathbf{z}; \boldsymbol{\mu}_{\phi}(\mathbf{x}), \mathbf{S}_{\phi}(\mathbf{x})) \quad (29)$$

where the covariance matrix is assumed to be diagonal i.e. $\mathbf{S}_{\phi}(\mathbf{x}) = \text{diag}(\boldsymbol{\sigma}_{\phi}^2(\mathbf{x}))$. Furthermore $\boldsymbol{\mu}_{\phi}(\mathbf{x})$ and $\log \boldsymbol{\sigma}_{\phi}^2(\mathbf{x})$ are taken as the outputs of the encoding neural networks $f_{\phi}^{\mu}(\mathbf{x})$ and $f_{\phi}^{\sigma}(\mathbf{x})$, respectively:

$$\boldsymbol{\mu}_{\phi}(\mathbf{x}) = f_{\phi}^{\mu}(\mathbf{x}) \quad \text{and} \quad \log \boldsymbol{\sigma}_{\phi}^2(\mathbf{x}) = f_{\phi}^{\sigma}(\mathbf{x}). \quad (30)$$

We provide further details later in this section along with the structure of the employed networks. In our model, we assume a diagonal Gaussian approximation for the posterior $q_{\phi}(\mathbf{z}|\mathbf{x})$. We are aware that the actual, but intractable, posterior $p_{\theta}(\mathbf{z}|\mathbf{x})$ could differ from a diagonal Gaussian and even from a multivariate normal distribution. However, the low variance $\boldsymbol{\sigma}_{\phi}^2$ observed in test cases justifies the assumption of a diagonal Gaussian in this context. An enriched model for the approximate posterior $q_{\phi}(\mathbf{z}|\mathbf{x})$ could rely on e.g. normalizing flows¹²¹. Recent developments on autoregressive flows¹²² overcome the practical restriction of normalizing flows to low-dimensional latent spaces.

As noted in Eq. (16), we employ the reparametrization trick by writing each random variable $\mathbf{z}^{(i,l)} \sim q_{\phi}(\mathbf{z}^{(i)}|\mathbf{x}^{(i)})$ as

$$\mathbf{z}^{(i,l)} = g_{\phi}(\mathbf{x}^{(i)}, \boldsymbol{\epsilon}^{(l)}) = \boldsymbol{\mu}_{\phi}(\mathbf{x}^{(i)}) + \boldsymbol{\sigma}_{\phi}(\mathbf{x}^{(i)}) \odot \boldsymbol{\epsilon}^{(l)}, \quad (31)$$

and

$$\boldsymbol{\epsilon}^{(l)} \sim p(\boldsymbol{\epsilon}) = \mathcal{N}(\mathbf{0}, \mathbf{I}), \quad (32)$$

where \odot denotes element-wise vector product.

We utilize the following structure for the decoding neural network $f_{\boldsymbol{\theta}}(\mathbf{z})$:

$$f_{\boldsymbol{\theta}}(\mathbf{z}) = \left(l_{\boldsymbol{\theta}}^{(4)} \circ \tilde{a}^{(3)} \circ l_{\boldsymbol{\theta}}^{(3)} \circ \tilde{a}^{(2)} \circ l_{\boldsymbol{\theta}}^{(2)} \circ \tilde{a}^{(1)} \circ l_{\boldsymbol{\theta}}^{(1)} \right) (\mathbf{z}). \quad (33)$$

The encoding networks for obtaining $\boldsymbol{\mu}_{\phi}(\mathbf{x})$ and $\boldsymbol{\sigma}_{\phi}^2(\mathbf{x})$ of the approximate posterior $q_{\boldsymbol{\theta}}(\mathbf{z}|\mathbf{x})$ share the structure,

$$f_{\phi}(\mathbf{x}) = \left(a^{(3)} \circ l_{\phi}^{(3)} \circ a^{(2)} \circ l_{\phi}^{(2)} \circ a^{(1)} \circ l_{\phi}^{(1)} \right) (\mathbf{x}), \quad (34)$$

which gives rise to $f_{\phi}^{\boldsymbol{\mu}}(\mathbf{x})$ and $f_{\phi}^{\boldsymbol{\sigma}}(\mathbf{x})$ with,

$$f_{\phi}^{\boldsymbol{\mu}}(\mathbf{x}) = l_{\phi}^{(4)}(f_{\phi}(\mathbf{x})) \quad \text{and} \quad f_{\phi}^{\boldsymbol{\sigma}}(\mathbf{x}) = l_{\phi}^{(5)}(f_{\phi}(\mathbf{x})). \quad (35)$$

In Eqs. (33)- (35), we consider linear layers $l^{(i)}$ of a variable \mathbf{y} with $l^{(i)}(\mathbf{y}) = \mathbf{W}^{(i)}\mathbf{y} + \mathbf{b}^{(i)}$ and non-linear activation functions denoted with $a(\cdot)$. The indices ϕ and θ of the linear layers $l^{(i)}$ reflect correspondence to either the encoding or decoding network, respectively. ϕ comprises all parameters of the encoding network $f_{\phi}^{\boldsymbol{\mu},\boldsymbol{\sigma}}(\mathbf{x})$, θ all parameters of the decoding network $f_{\theta}(\mathbf{z})$ including the parameters $\boldsymbol{\sigma}_{\theta}^2$ discussed in Eq. (27). We differentiate the encoding and decoding activation functions by denoting them as $a^{(i)}$ and $\tilde{a}^{(i)}$, respectively. All layers considered were fully connected. The general architecture of the neural networks employed and how these affect the objective $\mathcal{L}(\boldsymbol{\theta}, \phi; \mathbf{X})$ are depicted in Fig. 2.

The optimization of the objective is carried out by a stochastic gradient ascent algorithm. In our case, we employ ADAM⁹¹ with the parameters chosen as $\alpha = 0.001, \beta_1 = 0.9, \beta_2 = 0.999, \epsilon = 1.0\text{e}^{-8}$. Gradients of the lower-bound $\mathcal{L}(\boldsymbol{\theta}, \phi; \mathbf{X})$ with respect to the model parametrization $\{\phi, \theta\}$ are estimated by the backpropagation procedure¹¹⁸. The required gradients for optimizing the parameters $\boldsymbol{\sigma}_{\theta}^2$ can be computed analytically. For an entry $\sigma_{j,\theta}^2$,

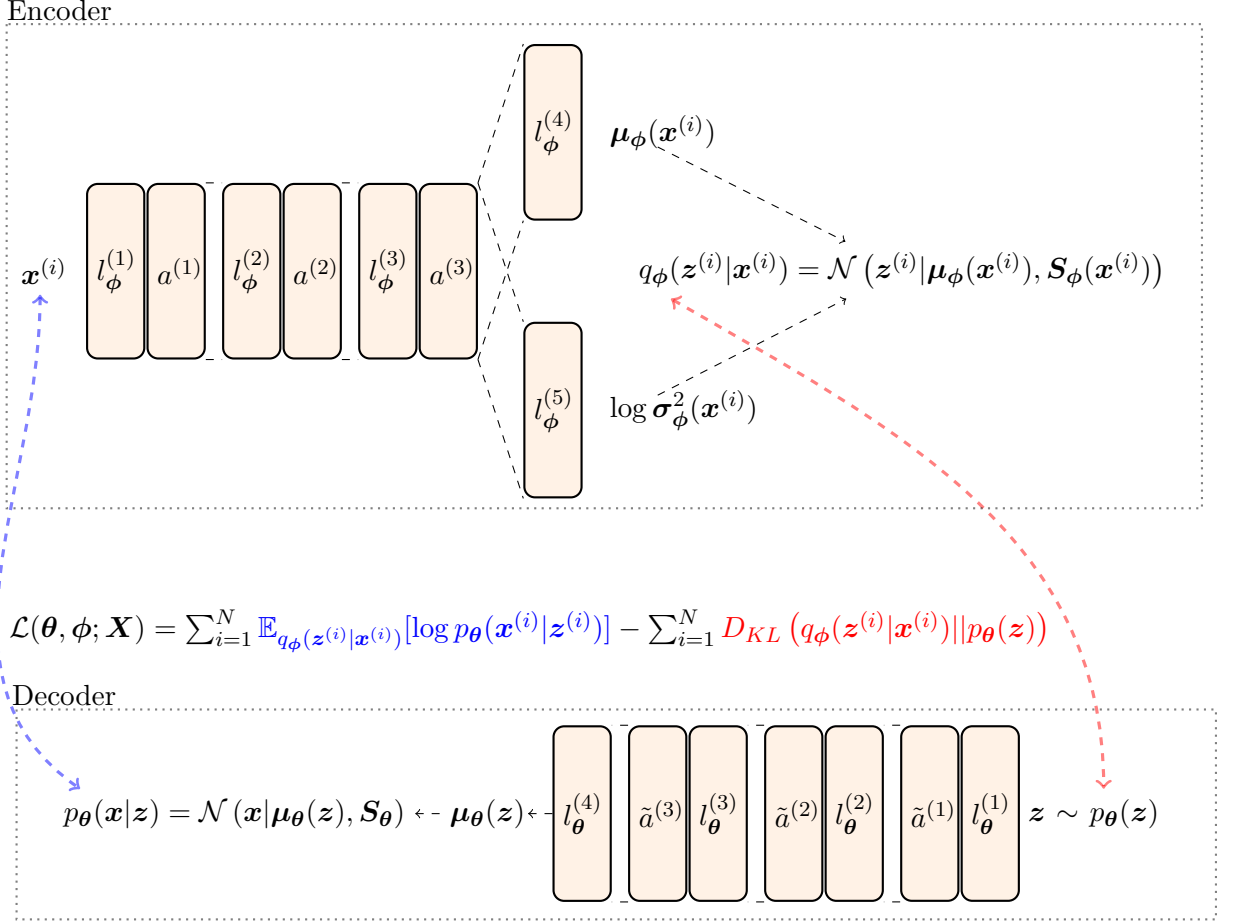


FIG. 2. Schematic of the AEVB depicting the employed network architecture. Fully connected linear layers are denoted with $l^{(i)}$ and non-linear activation functions with $a^{(i)}$. The indices ϕ and θ indicate encoding and decoding networks, respectively. The maximization of the lower-bound on the log-likelihood $\mathcal{L}(\theta, \phi; \mathbf{X})$ in Eq. (11) simultaneously optimizes the parametrization of the encoder and decoder. The first term in $\mathcal{L}(\theta, \phi; \mathbf{X})$ accounts for the reconstruction of the training data $\mathbf{x}^{(i)}$ with $\mathbf{z}^{(i)}$ distributed according $q_\phi(\mathbf{z}^{(i)}|\mathbf{x}^{(i)})$. The second term, in aggregation of all data $\mathbf{x}^{(i)}$, ensures that $q_\phi(\mathbf{z}^{(i)}|\mathbf{x}^{(i)})$ is close to $p(\mathbf{z})$.

Linear layer	Input dimension	Output dimension	Activation layer	Activation function
$l_{\phi}^{(1)}$	$\dim(\mathbf{x})$	d_1	$a^{(1)}$	SeLu ^a
$l_{\phi}^{(2)}$	d_1	d_2	$a^{(2)}$	SeLu
$l_{\phi}^{(3)}$	d_2	d_3	$a^{(3)}$	Log Sigmoid ^b
$l_{\phi}^{(4)}$	d_3	$\dim(\mathbf{z})$	None	-
$l_{\phi}^{(5)}$	d_3	$\dim(\mathbf{z})$	None	-

^a SeLu: $a(x) = \begin{cases} \alpha(e^x - 1) & \text{if } x < 0 \\ x & \text{otherwise.} \end{cases}$ See [123] for further details.

^b Log Sigmoid: $a(x) = \log \frac{1}{1+e^{-x}}$

TABLE I. Network specification of the encoding neural network with $d_1 = 50$, $d_2 = 100$, and $d_3 = 100$.

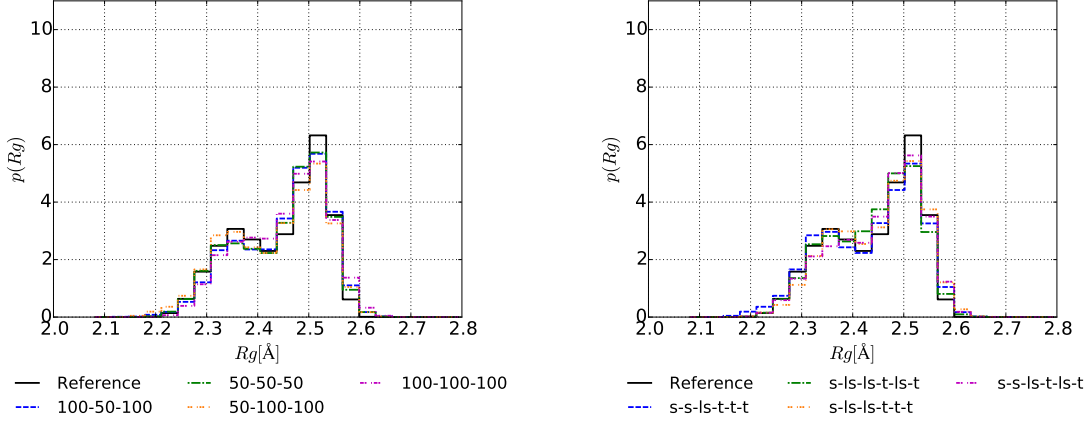
Linear layer	Input dimension	Output dimension	Activation layer	Activation function
$l_{\theta}^{(1)}$	$\dim(\mathbf{z})$	d_3	$\tilde{a}^{(1)}$	Tanh
$l_{\theta}^{(2)}$	d_3	d_2	$\tilde{a}^{(2)}$	Tanh
$l_{\theta}^{(3)}$	d_2	d_1	$\tilde{a}^{(3)}$	Tanh
$l_{\theta}^{(4)}$	d_1	$\dim(\mathbf{x})$	None	-

TABLE II. Network specification of the decoding neural network with $d_{\{1,2,3\}}$ as defined in Table I.

we can write the following:

$$\begin{aligned}
\frac{\partial \mathcal{L}(\boldsymbol{\theta}, \phi; \mathbf{x}^{(i)})}{\partial \log \sigma_{j,\boldsymbol{\theta}}^2} &= \frac{\partial \log p_{\boldsymbol{\theta}}(\mathbf{x}^{(i)}|\mathbf{z})}{\partial \log \sigma_{j,\boldsymbol{\theta}}^2} \\
&= \frac{\partial}{\partial \log \sigma_{j,\boldsymbol{\theta}}^2} \left(-\frac{1}{2} \sum_{j=1}^{\dim(\mathbf{x}^{(i)})} \frac{\left(x_j^{(i)} - \mu_{j,\boldsymbol{\theta}}(\mathbf{z})\right)^2}{\sigma_{j,\boldsymbol{\theta}}^2} \right) \\
&= \frac{\partial}{\partial \log \sigma_{j,\boldsymbol{\theta}}^2} \left(-\frac{1}{2} \sum_{j=1}^{\dim(\mathbf{x}^{(i)})} \frac{\left(x_j^{(i)} - \mu_{j,\boldsymbol{\theta}}(\mathbf{z})\right)^2}{\exp(\log(\sigma_{j,\boldsymbol{\theta}}^2))} \right) \\
&= \frac{1}{2} \frac{\left(x_j^{(i)} - \mu_{j,\boldsymbol{\theta}}(\mathbf{z})\right)^2}{\sigma_{j,\boldsymbol{\theta}}^2}.
\end{aligned} \tag{36}$$

Studying different combinations of activation functions and layers for the encoding network $f_{\phi}^{\mu,\sigma}(\mathbf{x})$ and decoding network $f_{\theta}(\mathbf{z})$ led to the network architecture depicted in Tables I



(a) Varying dimensionality of the layers $l_{\{\theta, \phi\}}^{(i)}$. The figure's labels represent the dimensionality of the layers in the format $d_1-d_2-d_3$ as specified in Tables I and II. We use the activation functions as denoted in the tables.

(b) Testing different activation functions for $a^{(i)}$. The labels specify the utilized activation functions in the following manner: $a^{(1)}-a^{(2)}-a^{(3)}-\tilde{a}^{(1)}-\tilde{a}^{(2)}-\tilde{a}^{(3)}$. We use the abbreviations: t: Tanh, s: SeLu, ls: Log Sigmoid.

FIG. 3. Prediction of the radius of gyration with differing networks, in terms of (a) the dimensionality of the layers and (b) regarding the type of activation functions used. Changes in the network specification lead to similar predictions. This model has been trained with a dataset of size $N = 500$.

and II, respectively. This network provided a repeatedly stable optimization during training. Variations of the given network architecture resulted into similar predictive capabilities as shown in Fig. 3. Increasing the dimension of \mathbf{z} did not improve the predictive capabilities as shown in Fig. 4. This implies that CVs with $\dim(\mathbf{z}) = 2$ suffice to capture the physics encapsulated in the ALA-2 dataset with $\dim(\mathbf{x}) = 66$.

3. Results

In the following illustrations, we trained the model by varying the number of snapshots N . We utilized a sub-sampled batch of size $M = 64$ from the dataset of size N . In cases where $N < 64$, we set $M = N$. The hyper parameters of the ARD prior in Eq. (19) are set to $a_0 = b_0 = 1.0e^{-5}$. Other values for a_0, b_0 in the range of $[1.0e^{-8}, 1.0e^{-4}]$ were also employed

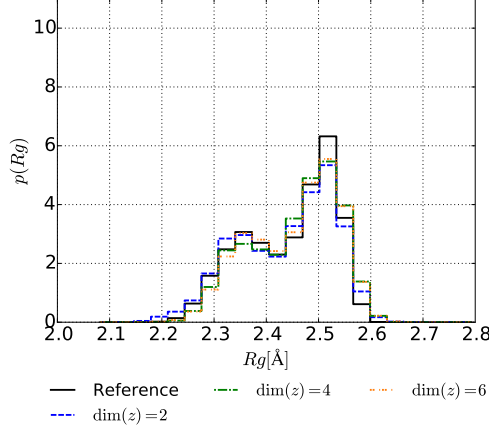


FIG. 4. Predicted radius of gyration for models utilizing different $\dim(\mathbf{z})$. The predictions are based on a model as specified in Tables I and II with $N = 500$.

without a significant effect on the obtained sparsity patterns or the predictive accuracy of the model.

Fig. 5 depicts the \mathbf{z} -coordinates of $N = 500$ training data as well as those of 1527 test data which have been classified into the three modes based on the values of the dihedral angles. In order to obtain the \mathbf{z} -coordinates of the test data we made use of the mean $\mu_\phi(\mathbf{x}^{(i)})$ of the inferred approximate posterior q_ϕ as obtained after training. The resulting picture essentially provides the pre-images of the atomistic configurations in the CV space. Interestingly, similar atomistic configurations, i.e. belonging to the same of the three modes, $\alpha, \beta-1, \beta-2$, are recognized by $q_\phi(\mathbf{z}|\mathbf{x})$ and mapped to clusters in the identified CV space. $\beta-1$ configurations are encoded by $q_\phi(\mathbf{z}|\mathbf{x})$ to regions with high probability mass in $p_\theta(\mathbf{z})$, i.e. CVs \mathbf{z} close to the center of $p_\theta(\mathbf{z}) = N(\mathbf{0}, \mathbf{I})$ are assigned. This is in accordance with the reference Boltzmann distribution $p(\mathbf{x})$ where $\beta-1$ is the most probable conformation.

Various dimensionality reduction methods are designed in order to keep similar \mathbf{x} close in their embedding on the lower-dimensional CV manifold, e.g., multidimensional scaling³⁰ or ISOMAP³³. In the presented scheme, the generative model learns that mapping similar \mathbf{x} to similar \mathbf{z} leads to an expressive (in terms of the likelihood) lower-dimensional representation. This similarity is revealed by inferring the approximate posterior $q_\phi(\mathbf{z}|\mathbf{x})$. Therefore, the desired similarity mentioned in [13] between configurations in the atomistic representation \mathbf{x} and via $q_\phi(\mathbf{z}|\mathbf{x})$ in the assigned CVs \mathbf{z} is achieved.

In contrast to several other dimensionality reduction techniques (e.g. Isomap³³ and Dif-

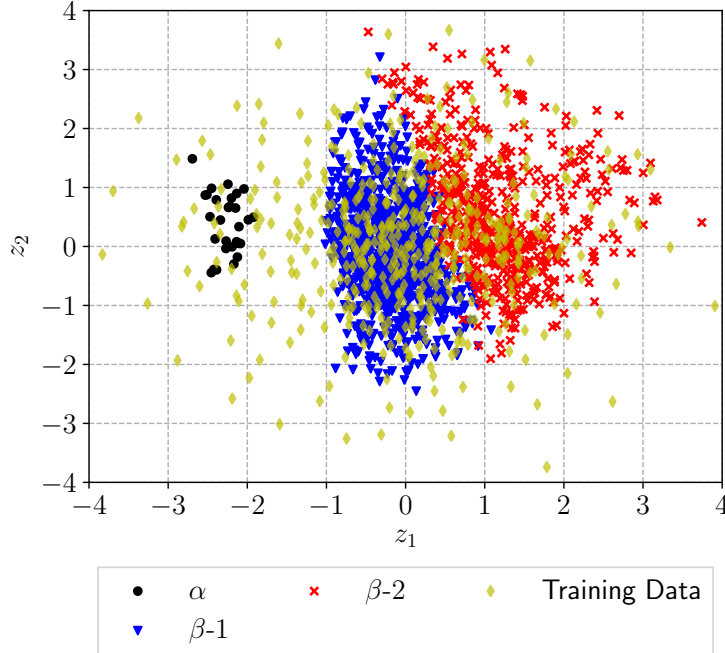


FIG. 5. Representation of the \mathbf{z} -coordinates of the training data \mathbf{X} with $N = 500$ in the CV space (yellow diamonds). Using the trained model and the mean of $q_\phi(\mathbf{z}|\mathbf{z})$ we computed the \mathbf{z} -coordinates of 1527 test samples corresponding to different conformations of the alanine dipeptide to α (black), β -1 (blue), and β -2 (red). Without any prior physical information, the encoder yields three distinct clusters in the CV space.

fusion maps^{38–40}), which as mentioned in the introduction require large amounts of training data e.g. $N > 10,000$ ^{13,49}, the proposed method can be perform quite well in the small data regimes, e.g. for $N = 50$ as it can be seen in Fig. 7. The latter depicts the Ramachandran plot in terms of the dihedral angles based on various amounts of training data N and compares it with the one predicted by the trained model on the same N as well as with the reference (obtained with $N = 10,000$). We note that the trained model yields Ramachandran plots that more closely resemble the reference as compared to the ones computed by the training data alone. The encoder, trained with $N = 200$, is capable of generating atomistic configurations leading to (ϕ, ψ) tuples which are not included in the training data.

The ARD prior advocated in Eq. (19) drives 58% of the parameters $\boldsymbol{\theta}$ to zero (as a threshold we consider a parameter to be inactive when its value drops below 1.0e^{-4}). In contrast, all network parameters $\boldsymbol{\theta}$ remain active while optimizing the objective without the ARD prior. Apart from the qualitative advantage, the sparsity-inducing prior provides a strong

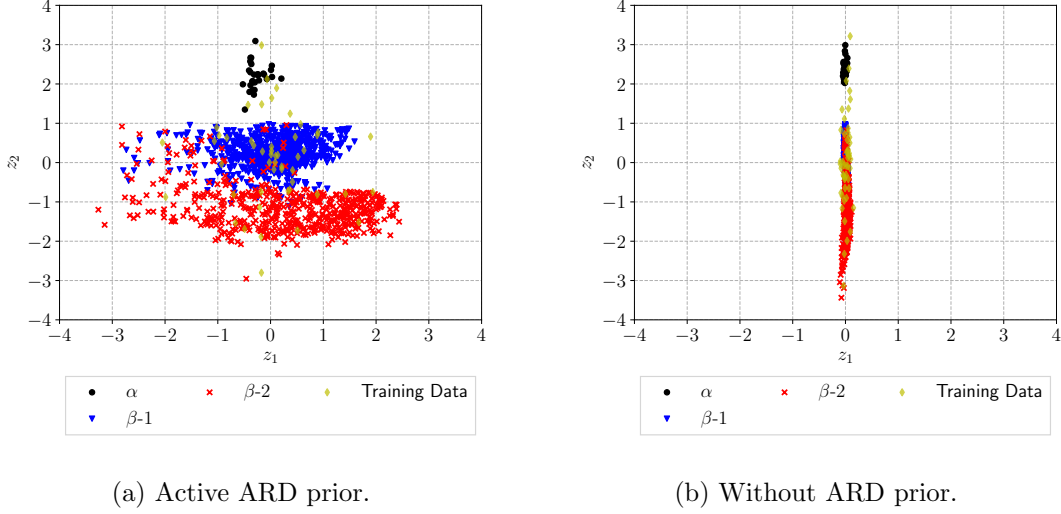


FIG. 6. Representation of the \mathbf{z} -coordinates of the training data \mathbf{X} with $N = 50$ in the CV space (yellow diamonds). Using the trained model and the mean of $q_\phi(\mathbf{z}|\mathbf{z})$ we computed the \mathbf{z} -coordinates of 1527 test samples corresponding to different conformations of the alanine dipeptide to α (black), β -1 (blue), and β -2 (red). In the case of limited training data, the ARD prior facilitates the identification of physically meaningful CVs (left) compared to the representation on the right obtained without the ARD prior. Note that the changed positioning of the conformations in the CV space compared to Fig. 5 is due to symmetries in $p_\theta(\mathbf{z})$.

regularization in the presence of limited data and yields superior predictive estimates. In addition to obtaining sparse solutions, the ARD prior facilitates the identification of physically meaningful latent representations for limited data (e.g. $N = 50$) as shown in Fig. 6. Without the ARD prior, the data is encoded in a rather small region of the latent space.

In Fig. 8 we attempt to provide insight on the physical meaning of the CVs \mathbf{z} identified. In particular, we plot the atomistic configurations \mathbf{x} corresponding to various values of the first CV z_1 and while the second CV $z_2 = 0$. The conformational transition in predicted atomistic configurations can be clearly recognized in the peptides of Fig. 8. We note that we start on the left ($z_1 < 0$) with α configurations, then move towards β -1 (starting at $z_1 \approx -1$), and finally obtain β -2 configurations. For illustration purposes, the predictions in Fig. 8 are based solely on the mean $\boldsymbol{\mu}_\theta(\mathbf{z})$ of the probabilistic decoder $p_\theta(\mathbf{x}|\mathbf{z}) = \mathcal{N}(\mathbf{x}; \boldsymbol{\mu}_\theta(\mathbf{z}), \mathbf{S}_\theta = \text{diag}(\boldsymbol{\sigma}_\theta^2))$. We note that for each value of the CVs \mathbf{z} several atomistic realizations \mathbf{x} can be drawn from $p_\theta(\mathbf{x}|\mathbf{z})$ as depicted in Fig. 9. This figure reveals the characteristic and relevant movement of the backbone that is captured by the predictive mean $\boldsymbol{\mu}_\theta(\mathbf{z}) = f_\theta^\mu(\mathbf{z})$.

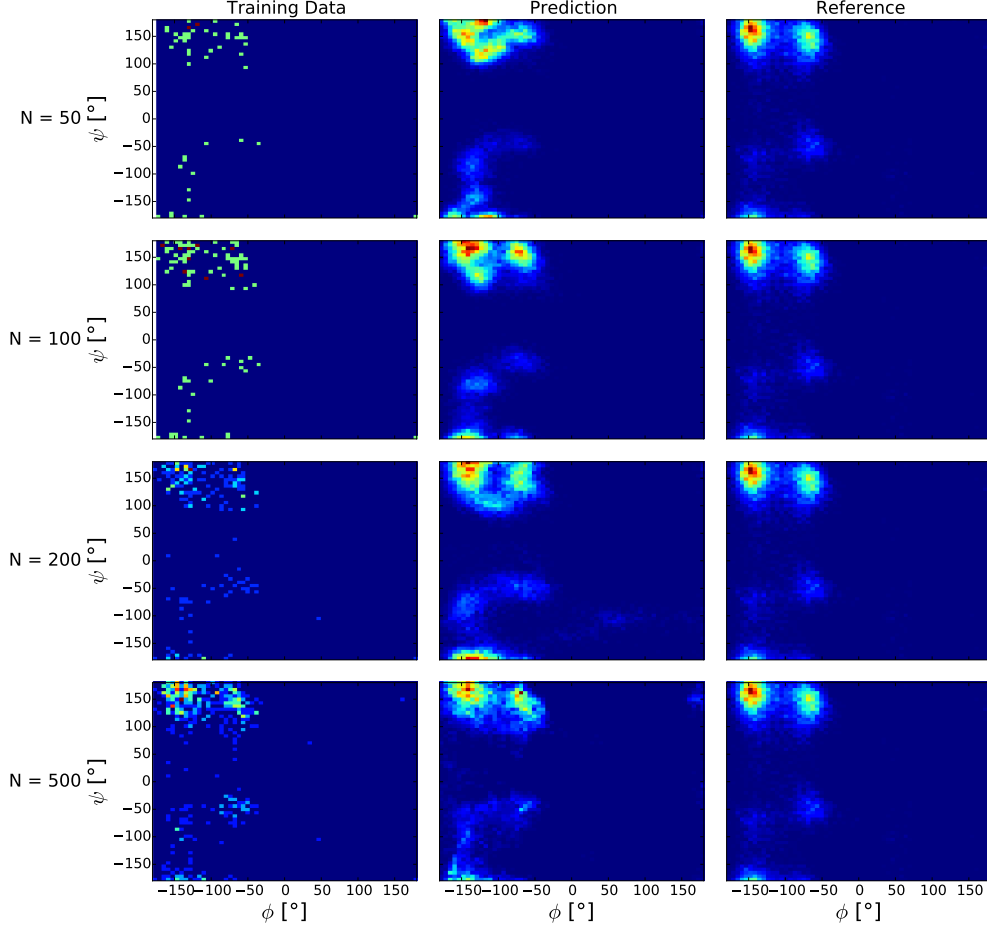


FIG. 7. Ramachandran plot estimated with the training data \mathbf{X} (left column), using predictions of the trained model (middle column), and the reference (right column, estimated with $N = 10,000$). Each row refers to different size N of training datasets (the figure on the right column is repeated to allow easy comparison with the results on the first two columns). The represented predictions are obtained by applying Algorithm [2] with $T = 10,000$ samples. The generative nature of the model allows more accurate estimates than when using the training data alone. In addition, the Bayesian approach allows for predictions with their associated uncertainties as discussed subsequently.

Fluctuations of less relevant outer Hydrogen atoms (see Figs. [9(b)-9(d)]) are recognized as noise of the decoder $p_{\theta}(\mathbf{x}|\mathbf{z}) = \mathcal{N}(\boldsymbol{\mu}(\mathbf{z}), \mathbf{S}_{\theta} = \text{diag}(\boldsymbol{\sigma}_{\theta}^2))$ denoted in Eq. (27). We note also that the corresponding entries of $\boldsymbol{\sigma}_{\theta}$ responsible for the outer Hydrogen atoms are five times larger compared to the remaining atoms. The proposed model can therefore in unsupervised fashion identify the central role of the backbone coordinates whereas this physical insight is pre-assumed in [8 and 67].

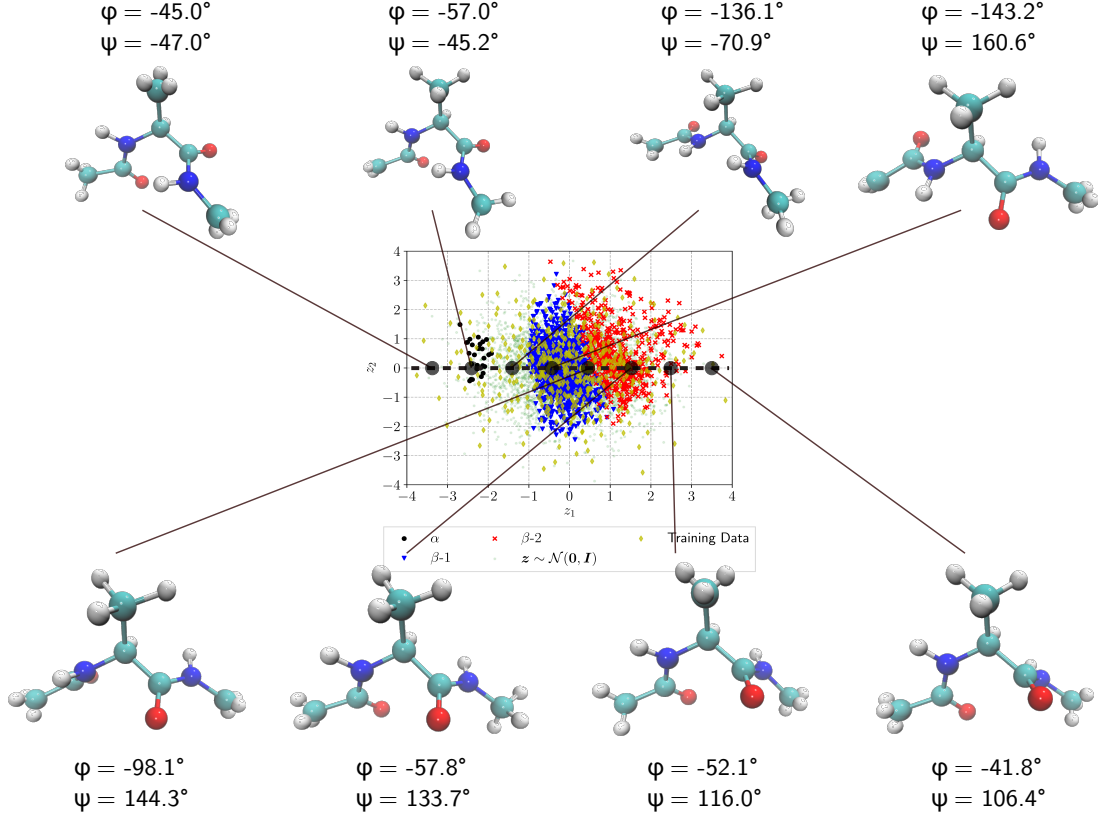
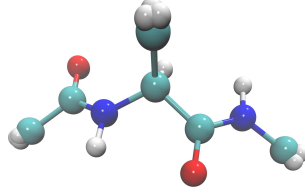


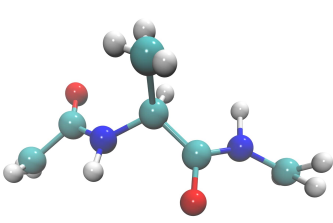
FIG. 8. *Predicted* configurations \mathbf{x} (including dihedral angle values) for $\{\mathbf{z} | z_1 = \{-3.5, -2.5, \dots, 3.5\}, z_2 = 0\}$ with $\mu_\theta(\mathbf{z})$ of $p_\theta(\mathbf{x} | \mathbf{z})$. As one moves along the z_1 axis, we obtain for the given CVs atomistic configurations \mathbf{x} reflecting the conformations α , $\beta-1$, and $\beta-2$. Rendered atomistic representations are created by VMD¹²⁴.

In order to gain further insight into the relation between the dihedral angles ϕ, ψ and the discovered CVs \mathbf{z} , we plot in Figures Fig. 5 and Fig. 10 the corresponding maps for various combinations of \mathbf{z} -values. While it is clear that the map is not always bijective, the figures reveal the strong correlation between the two sets of variables. It should also be noted that in contrast to the dihedral angles, the \mathbf{z} value for a given atomistic configuration \mathbf{x} are not unique but rather there is a whole distribution as implied by $q_\phi(\mathbf{z} | \mathbf{x})$. For the aforementioned plots we computed the \mathbf{z} from the mean of this density i.e. $\mu_\phi(\mathbf{x})$.

The trained model can also be employed in computing predictive estimates of observables $\int a(\mathbf{x}) p_{target}(\mathbf{x}) d\mathbf{x}$ by making using of $\bar{p}_\theta(\mathbf{x})$ and samples drawn from it as described in

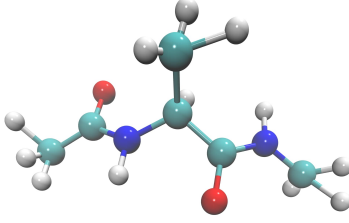


(a) Mean prediction $\boldsymbol{\mu}_\theta(\mathbf{z}^0)$ for a sample $\mathbf{z}^0 \sim p(\mathbf{z})$.



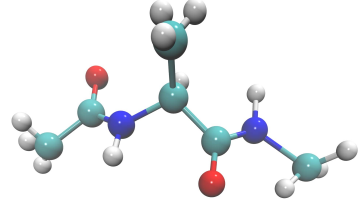
(b) Realization $\mathbf{x}^{0,0} \sim$

$$p_\theta(\mathbf{x}|\boldsymbol{\mu}_\theta(\mathbf{z}^0), \mathbf{S}_\theta = \text{diag}(\boldsymbol{\sigma}_\theta^2)).$$



(c) Realization $\mathbf{x}^{1,0} \sim$

$$p_\theta(\mathbf{x}|\boldsymbol{\mu}_\theta(\mathbf{z}^0), \mathbf{S}_\theta = \text{diag}(\boldsymbol{\sigma}_\theta^2)).$$



(d) Realization $\mathbf{x}^{2,0} \sim$

$$p_\theta(\mathbf{x}|\boldsymbol{\mu}_\theta(\mathbf{z}^0), \mathbf{S}_\theta = \text{diag}(\boldsymbol{\sigma}_\theta^2)).$$

FIG. 9. Visualization of the mean prediction (a) for a sample $\mathbf{z}^0 \sim p(\mathbf{z})$, obtained from the decoding network $\boldsymbol{\mu}_\theta(\mathbf{z}^0) = f_\theta(\mathbf{z}^0)$, and realizations (b-d) $\mathbf{x}^{j,0} \sim p_\theta(\mathbf{x}|\mathbf{z}^0)$. Less relevant positions of the outer Hydrogen atoms are captured by the noise $\boldsymbol{\sigma}_\theta$ of the model $p_\theta(\mathbf{x}|\mathbf{z}^0) = \mathcal{N}(\boldsymbol{\mu}(\mathbf{z}_\theta^0), \mathbf{S}_\theta = \text{diag}(\boldsymbol{\sigma}_\theta^2))$.

section II D. We illustrate this here by computing the radius of gyration (Rg)^{105,125} given as,

$$a_{\text{Rg}}(\mathbf{x}) = \sqrt{\frac{\sum_p m_p \|\mathbf{x}_p - \mathbf{x}_{\text{COM}}\|^2}{\sum_p m_p}}. \quad (37)$$

The sum in Eq. (37) considers all atoms $p = 1, \dots, P$ of the peptide, where m_p and \mathbf{x}_p denote the mass and the coordinates of each atom, respectively. \mathbf{x}_{COM} denotes the center of mass of the peptide. The histogram of $a_{\text{Rg}}(\mathbf{x})$ reflects the distribution of the size of the peptide and is correlated with the various conformations¹²⁵.

In the estimates that we depict in Fig. 12 we have also employed the posterior approximation of $\boldsymbol{\theta}$ obtained as described in section II F in order to compute credible intervals for the observable. These credible intervals are estimated as described in Algorithm [3] from $J = 3000$ samples. We observe that the model's confidence in its prediction increases with the size of the training data. This is reflected in shrinking credible intervals in Fig. 12 for increasing N .

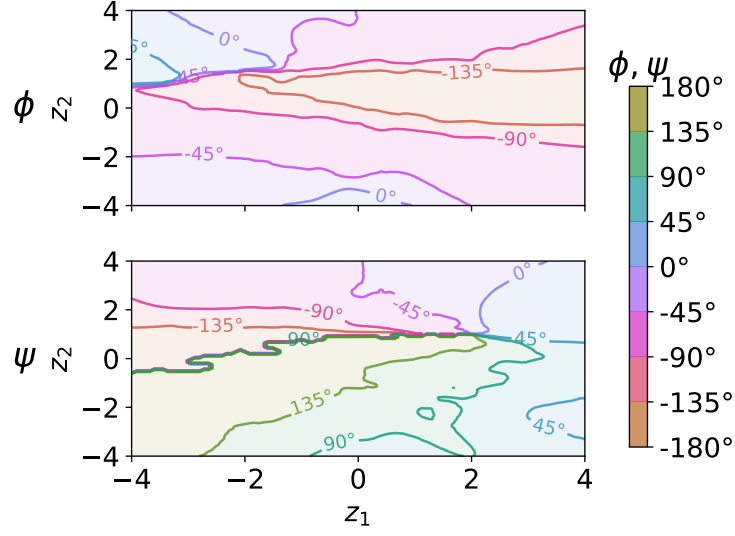


FIG. 10. Predicted dihedral angles (ϕ, ψ) given the latent variables $\mathbf{z} \in [-4, 4]^2$.

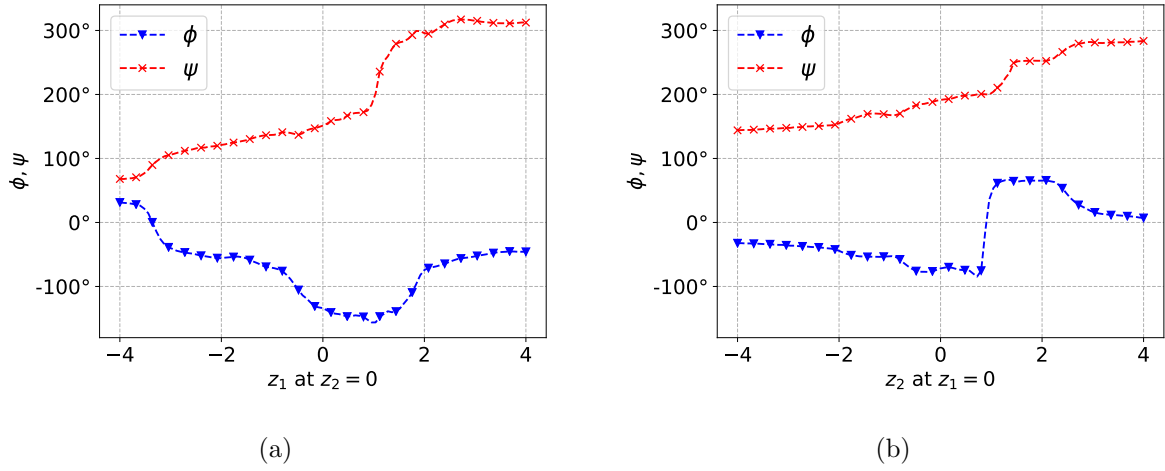


FIG. 11. Predicted dihedral angles (ϕ, ψ) given the latent variables (a) $\{z_1, z_2 | z_1 \in [-4, 4], z_2 = 0\}$ and (b) $\{z_1, z_2 | z_1 = 0, z_2 \in [-4, 4]\}$.

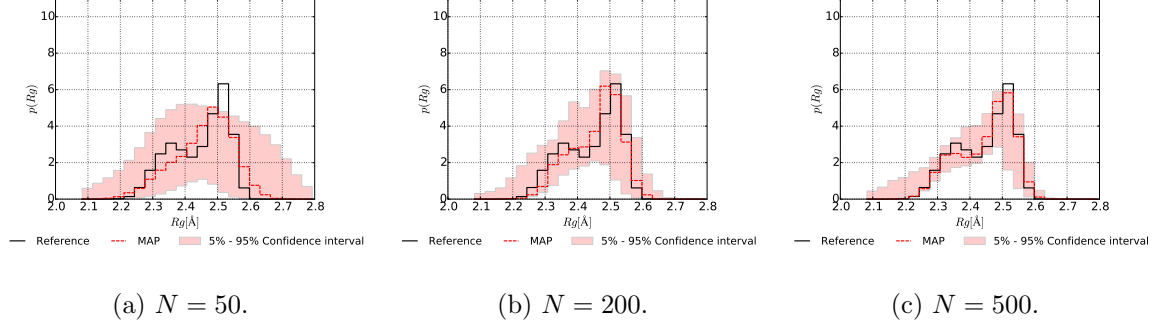


FIG. 12. Predicted radius of gyration with $\dim(\mathbf{z}) = 2$ for various sizes N of the training dataset. The MAP estimate indicated in red is compared to the reference (black) solution. The latter is estimated by $N = 10,000$. The shaded area represents the 5%-95% confidence interval, reflecting the induced epistemic uncertainty from the limited amount of training data.

Algorithm 3 Estimating credible intervals.

Input J = number of samples to be drawn, optimal values of $\boldsymbol{\theta} = \boldsymbol{\theta}_{MAP}$ and $\phi = \phi_{MAP}$.

Compute Laplace's approximation $\mathcal{N}(\boldsymbol{\mu}_L, \mathbf{S}_L = \text{diag}(\boldsymbol{\sigma}_L^2))$ to the posterior $p(\boldsymbol{\theta}|\mathbf{X})$ (Eq. (23)).

for $j = 1$ **to** J **do**

Draw a posterior sample: $\boldsymbol{\theta}^j \sim \mathcal{N}(\boldsymbol{\mu}_L, \mathbf{S}_L = \text{diag}(\boldsymbol{\sigma}_L^2))$.

Obtain a predictive trajectory $\bar{\mathbf{x}}_{1:T}^j$, given the parametrization $\boldsymbol{\theta}^j$. See Algorithm [2].

Estimate the observable $\hat{a}(\boldsymbol{\theta}^j) = \frac{1}{T} \sum_{t=1}^T a(\bar{\mathbf{x}}_t^j)$, given the trajectory $\bar{\mathbf{x}}_{1:T}^j$.

end for

Estimate the desired quantiles with $\hat{a}(\boldsymbol{\theta}^{1:J})$.

In summary for ALA-2, we note that the proposed methodology for identifying CVs (Fig. 5) and predicting observables (Fig. 7 and Fig. 12) works well with small size datasets e.g. $N = \{50, 200, 500\}$.

B. ALA-15

1. Simulation of ALA-15 and model specification

The following example considers a larger alanine peptide with 15 residues, ALA-15 which consists of 162 atoms giving rise to $\dim(\mathbf{x}) = 486$. The reference dataset \mathbf{X} has been obtained in similar manner as specified in Section III A 1 with the only difference being

that we utilize a replica-exchange molecular dynamics¹²⁶ algorithm with 21 temperature replicas distributed according $T_i = T_0 e^{\kappa \cdot i}$ ($T_0 = 270$ K, and $\kappa = 0.04$). This leads to an analogous simulation setting as employed in [105]. The datasets are obtained as mentioned in the previous example. We consider here $N = \{300, 3000, 5000\}$. Using the same model specifications as in Section III A 2, we present next a summary of the obtained results.

2. Results

For visualization purposes of the latent CV space, we assumed $\dim(\mathbf{z}) = 2$ in the following, even though the presence of 15 residues each requiring a pair of dihedral angles (ϕ, ψ) would potentially suggest a higher-dimensional representation. However, when considering test cases with $\dim(\mathbf{z}) = \{15, 30\}$, no significant differences were observed in the predictive capabilities. The (ϕ, ψ) pairs within a peptide chain show high correlation. Multilayer neural networks provide the capability of transforming independent CVs (as considered in this study) to correlated ones by passing them through the subsequent network layers. This explains the reasonable predictive quality of the model using independent and low-dimensional CVs with $\dim(\mathbf{z}) = 2$. Considering more expressive $p_{\boldsymbol{\theta}}(\mathbf{z})$ than the standard Gaussian employed, could have accounted (in part) for such correlations. In this example, by employing the advocated ARD prior, only 43% of the decoder parameters $\boldsymbol{\theta}$ remained effective.

Figure Fig. 13 depicts the posterior means of the $N = 3,000$ training data in the CV space \mathbf{z} . Given that a peptide configuration contains residues from different conformations labelled here as α , β -1, and β -2 and residues in intermediate (ϕ, ψ) states, we applied the following rule for labelling/coloring each datapoint. The assigned color in Fig. 13 is a mixture between the RGB colors black (for α), blue (for β -1), and red (for β -2). The mixture weights of the assigned color are proportional to the number of residues belonging to the α (black), β -1 (blue), and β -2 (red) conformations, normalized by the total amount of residues which can be clearly assigned to α , β -1, and β -2. Additionally, we visualize the amount of intermediate (ϕ, ψ) states of the residues by the opacity of the scatter points. The opacity reflects the amount of residues which are clearly assigned to the α , β -1, and β -2 conformations compared to the total amount of residues in the peptide. For example, if all residues of a peptide configuration correspond to a specific mode, the opacity is taken as 100%. If all residues are in non-classified intermediate states, the opacity is set to the

minimal value which is here taken as 20%.

We note that peptide configurations in which the majority of residues belong to β -1 (blue) or in the β -2 conformation (red), are fairly clearly separated in the CV space from datapoints with residues predominantly in the α conformation (black). Nevertheless, we observe that the encoder has difficulties separating blue (β -1) and red (β -2) datapoints. We remark though that the related secondary structures¹²⁷ resulting from the assembly of residues in β -1 and β -2, such as the β -sheet and β -hairpin, share a similar atomistic representation \mathbf{x} which explains the similarity in the CV space.

When one moves in the CV space \mathbf{z} along the path indicated by a red dashed line in Fig. 14 and reconstructs the corresponding \mathbf{x} using the mean function of the decoder $p_{\theta}(\mathbf{x}|\mathbf{z})$, we obtain atomistic configurations of the ALA-15 partially consisting of the conformations α , β -1, and β -2 which correspond to the aforementioned secondary structures i.e. β -sheet (top left), β -hairpin (top middle and right), and α -helix (bottom row).

The ambiguity between β -1 and β -2 states is also reflected in the predicted Ramachandran plot in Fig. 15. Nevertheless properties, independent of the explicit separation of configurations predominantly consisting of residues in β -1 and β -2 states, are predicted accurately by the framework. This is demonstrated with the computed radius of gyration in Fig. 16. The MAP estimate is complemented by the credible intervals which reflect the epistemic uncertainty and are able to envelop the reference profile. As in the previously example, the breadth of the credible intervals shrinks with increasing training data N .

IV. CONCLUSIONS

We presented an unsupervised learning scheme for discovering CVs of atomistic systems. We defined the CVs as latent generators of the atomistic configurations and formulated their identification as a Bayesian inference task. Inference of the posterior distribution of the latent CVs given the fine-scale atomistic training data identifies a probabilistic mapping from the space of atomistic configurations to the latent space. This posterior distribution resembles a dictionary translating atomistic configurations to the lower-dimensional CV space which is inferred during the training procedure. Compared to other dimensionality reduction methods, the proposed scheme is capable of performing well with comparably heterogeneous and small datasets.

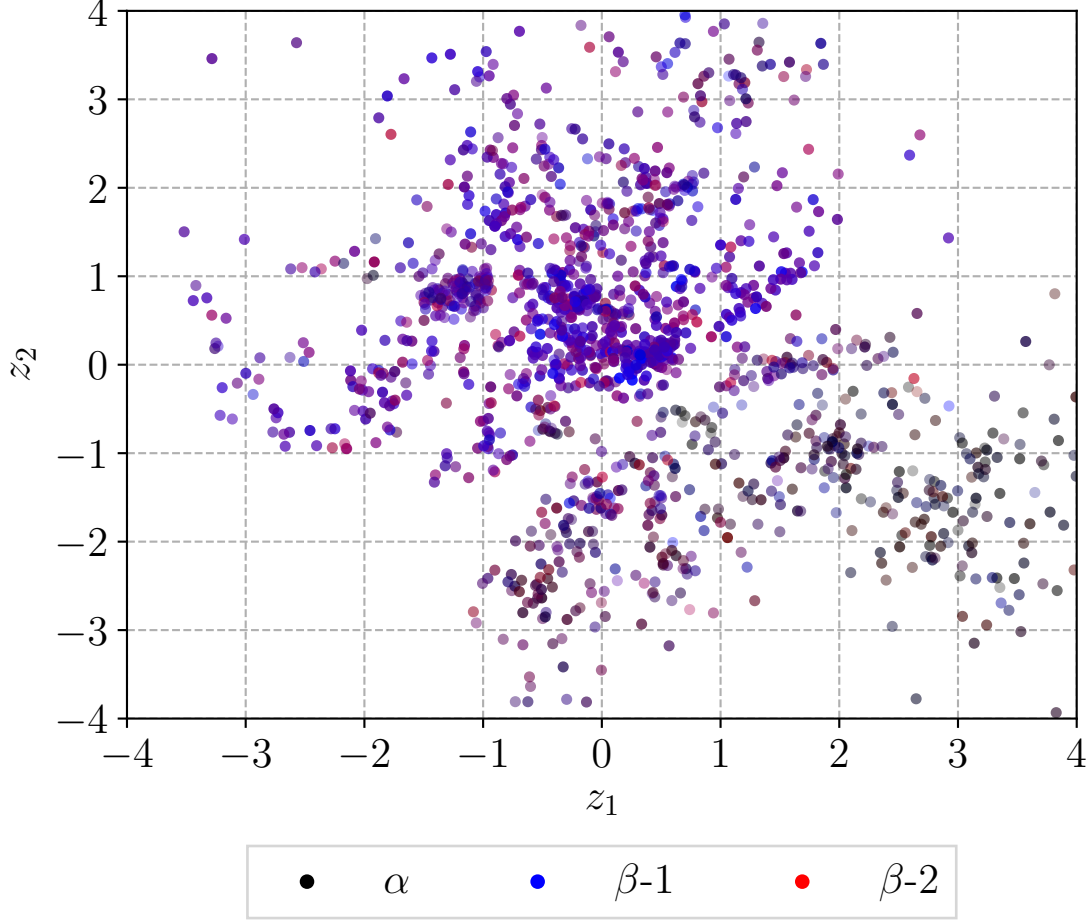


FIG. 13. Representation of the training data \mathbf{X} with $N = 3,000$ in the encoded collective variable space. The inferred approximate posterior $q_\phi(\mathbf{z}|\mathbf{x})$ separates residues mostly belonging to the β conformations (mixture of red and blue) and peptide configurations containing largely residues in the α configuration (black). Here, the mean $\boldsymbol{\mu}_\phi(\mathbf{x})$ of the approximate posterior $q_\phi(\mathbf{z}|\mathbf{x}) = \mathcal{N}(\mathbf{x}; \boldsymbol{\mu}_\phi(\mathbf{x}), \mathbf{S}_\phi = \text{diag}(\boldsymbol{\sigma}_\phi^2(\mathbf{x})))$ is depicted.

We presented the capabilities of the model for the test case of an ALA-2 peptide (Section III). When the dimensionality of the CVs $\dim(\mathbf{z}) = 2$ was set to 2, the model discovered variables that correlates strongly with the widely known dihedral angles (ϕ, ψ) . Other dimensionality reduction methods^{26,30,31,33,38–40} rely on an objective keeping small distances between configurations in the atomistic space also small in the latent space. Rather than enforcing this requirement directly, the proposed framework identifies a lower-dimensional representation that clusters configurations in the CV space which show similarities in the atomistic space. The Bayesian formulation presented allows for a rigorous quantification

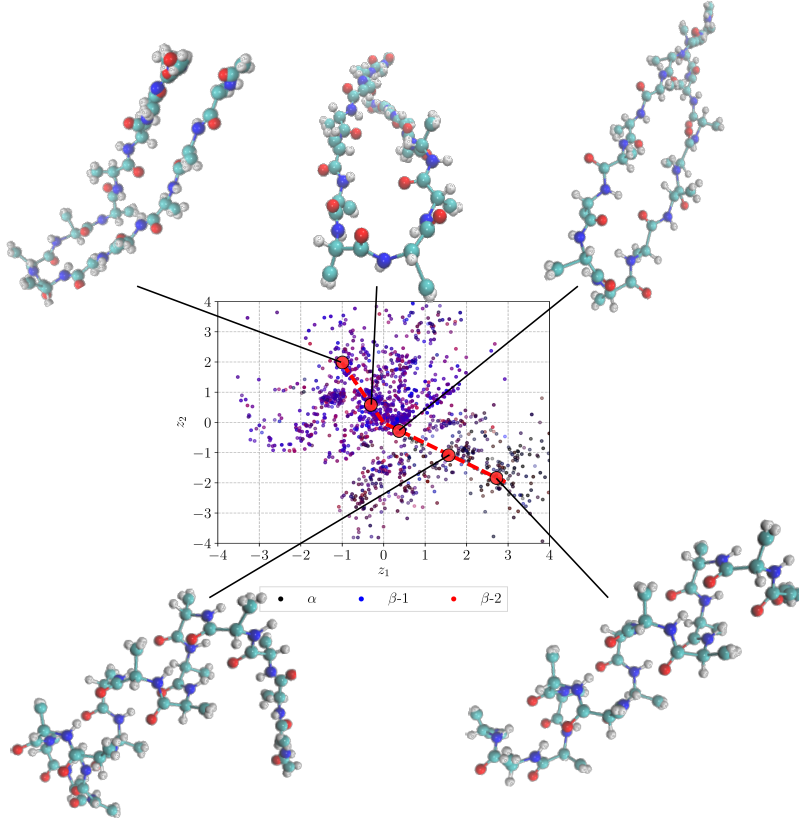


FIG. 14. *Predicted* configurations \mathbf{x} for decoding CVs indicated as red points on the dashed line in the plot. Depicted configurations have been produced by evaluating the $\mu_{\theta}(\mathbf{z})$ of $p_{\theta}(\mathbf{x}|\mathbf{z})$. Moving along the path, we obtain atomistic configurations \mathbf{x} partially consisting of the conformations α , β -1, and β -2 in the ALA-15 peptide resulting into peptide secondary structures such as β -sheet (top left), β -hairpin (top middle and right), and α -helix (bottom row). Rendered atomistic representations are created by VMD¹²⁴.

of the unavoidable uncertainties and their propagation in the predicted observables. The ARD prior chosen was shown to lead to on average 50% less parameters compared to the optimization without it.

We presented an approach for approximating the intractable posterior of the decoding model parameters (Eq. (23)) and provided an algorithm (Algorithm [3]) for estimating credible intervals. The uncertainty propagated to the observables captures the parameter uncertainty of the decoding neural network $f_{\theta}(\mathbf{z})$.

In addition to discovering CVs, the generative model employed, is able to predict atomistic configurations by sampling the CV space with $p_{\theta}(\mathbf{z})$ and mapping the CVs probabilistically

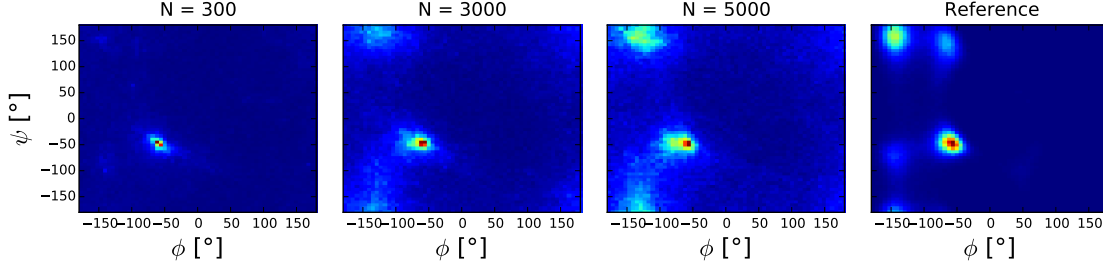


FIG. 15. Predicted Ramachandran plot with $\dim(\mathbf{z}) = 2$ for various sizes N of the training dataset (first three plots from the left). Depicted predictions are MAP estimates based on $T = 10,000$ samples. The plot on the right is the reference MD prediction with $N = 10,000$ configurations.

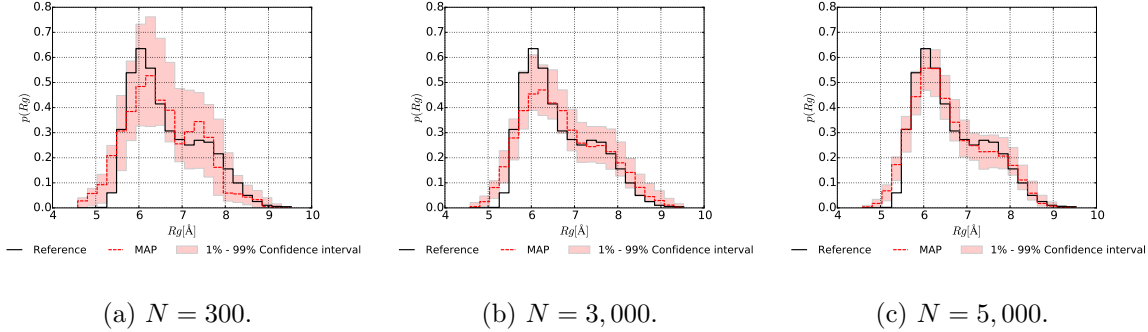


FIG. 16. Predicted radius of gyration with $\dim(\mathbf{z}) = 2$ for various sizes N of the training dataset. The MAP estimate indicated in red is compared to the reference (black) solution. The latter is estimated by $N = 10,000$. The shaded area represents the 1%-99% confidence interval, reflecting the induced epistemic uncertainty from the limited amount of training data.

via $p_{\theta}(\mathbf{x}|\mathbf{z})$ to full atomistic configurations. We showed that the predictive mapping $p_{\theta}(\mathbf{x}|\mathbf{z})$ recognizes essential backbone behavior of the peptide while it models fluctuations of the outer Hydrogen atoms with the noise of $p_{\theta}(\mathbf{x}|\mathbf{z})$ (see Fig. 9). We use the model for predicting observables with uncertainty quantification arising from using limited training data.

We emphasize that the whole work was based on data represented by Cartesian coordinates \mathbf{x} of all the atoms of the ALA-2 ($\dim(\mathbf{x}) = 66$) and ALA-15 ($\dim(\mathbf{x}) = 486$) peptides. Considering a pre-processed dataset e.g. by considering solely coordinates of the backbone atoms, heavy atom positions, or a representation by dihedral angles assumes the availability of tremendous physical insight. The aim of this work was to revealing CVs with physico-chemical meaning and the prediction of observables of complex systems without using any domain-specific physical notion.

Besides the framework proposed, generative adversarial networks (GANs)¹²⁸ and its Bayesian reformulation in [129] open an additional promising avenue in the context of CV discovery and enhanced sampling of atomistic systems. GANs are accompanied by a two player (generator and discriminator) min-max objective which poses known difficulties in training the model. The training of GANs is not as robust as the VAE employed here and Bayesian formulations are not well studied. In addition, one needs to address the mode collapse issue (see [130]) that is critical for atomistic systems.

Future work involves the use of the CVs discovered in the context of enhanced sampling techniques that can lead to an accelerated exploration of the configurational space. In addition to identifying the good CVs, a crucial step for enhanced sampling methods is the biasing potential for lifting deep free-energy wells. In contrast to the ideas e.g. presented in [8, 9, 131], we would advocate a formulation where the biasing potential is based on the lower-dimensional pre-image of the currently visited free-energy surface. To that end we envision using the posterior distribution $q_\phi(\mathbf{z}|\mathbf{x})$ to construct a locally optimal biasing potential defined in the CV space which gets updated on the fly as the simulations explore the configuration space. The biasing potential can be transformed by the probabilistic mapping of the generative model $p_\theta(\mathbf{x}|\mathbf{z})$ to the atomistic description as follows,

$$U_{\text{bias}}^{\mathbf{x}^{(i)}}(\mathbf{x}) \propto -\log \int_{\mathcal{M}_{CV}} p_\theta(\mathbf{x}|\mathbf{z}) q_\phi(\mathbf{z}|\mathbf{x}^{(i)}) d\mathbf{z}. \quad (38)$$

Eq. [38] is differentiable with respect to atomistic coordinates. Subtracting it from the atomistic potential as long as the approximation of the generative model is adequate could potentially accelerate the simulation by "filling-in" the deep free-energy wells.

ACKNOWLEDGEMENTS

The authors acknowledge support from the Defense Advanced Research Projects Agency (DARPA) under the Physics of Artificial Intelligence (PAI) program. M.S. acknowledges the non-material and financial support of the Hanns-Seidel-Foundation, Germany funded by the German Federal Ministry of Education and Research. His support by the Technical University of Munich is likewise acknowledged.

REFERENCES

- ¹J. R. Perilla, B. C. Goh, C. K. Cassidy, B. Liu, R. C. Bernardi, T. Rudack, H. Yu, Z. Wu, and K. Schulten, *Current Opinion in Structural Biology* **31**, 64 (2015), theory and simulation/Macromolecular machines and assemblies.
- ²P. Koutsourelakis, N. Zabaras, and M. Girolami, *Journal of Computational Physics* **321**, 1252 (2016).
- ³A. Barducci, M. Bonomi, and M. Parrinello, *Wiley Interdisciplinary Reviews: Computational Molecular Science* **1**, 826 (2011).
- ⁴F. Pietrucci and W. Andreoni, *Phys. Rev. Lett.* **107**, 085504 (2011).
- ⁵A. L. Ferguson, A. Z. Panagiotopoulos, P. G. Debenedetti, and I. G. Kevrekidis, *The Journal of Chemical Physics* **134**, 135103 (2011), <https://doi.org/10.1063/1.3574394>.
- ⁶W. Zheng, M. A. Rohrdanz, and C. Clementi, *The Journal of Physical Chemistry B* **117**, 12769 (2013), pMID: 23865517, <https://doi.org/10.1021/jp401911h>.
- ⁷O. Valsson and M. Parrinello, *Phys. Rev. Lett.* **113**, 090601 (2014).
- ⁸W. Chen and A. L. Ferguson, “Molecular enhanced sampling with autoencoders: On-the-fly collective variable discovery and accelerated free energy landscape exploration,” (2017), arXiv:1801.00203.
- ⁹P.-Y. Chen and M. E. Tuckerman, *The Journal of Chemical Physics* **148**, 024106 (2018), <https://doi.org/10.1063/1.4999447>.
- ¹⁰A. Mitsutake, Y. Mori, and Y. Okamoto, “Enhanced sampling algorithms,” in *Biomolecular Simulations: Methods and Protocols*, edited by L. Monticelli and E. Salonen (Humana Press, Totowa, NJ, 2013) pp. 153–195.
- ¹¹C. Bierig and A. Chernov, *Journal of Computational Physics* **314**, 661 (2016).
- ¹²J. Luque and X. Barril, eds., *Physico-Chemical and Computational Approaches to Drug Discovery*, RSC Drug Discovery (The Royal Society of Chemistry, 2012) pp. FP001–418.
- ¹³M. A. Rohrdanz, W. Zheng, and C. Clementi, *Annual Review of Physical Chemistry* **64**, 295 (2013), pMID: 23298245, <https://doi.org/10.1146/annurev-physchem-040412-110006>.
- ¹⁴G. Torrie and J. Valleau, *Journal of Computational Physics* **23**, 187 (1977).
- ¹⁵A. F. Voter, *The Journal of Chemical Physics* **106**, 4665 (1997), <https://doi.org/10.1063/1.473503>.

- ¹⁶D. Hamelberg, J. Mongan, and J. A. McCammon, *The Journal of Chemical Physics* **120**, 11919 (2004), <https://doi.org/10.1063/1.1755656>.
- ¹⁷T. Huber, A. E. Torda, and W. F. van Gunsteren, *Journal of Computer-Aided Molecular Design* **8**, 695 (1994).
- ¹⁸H. Grubmüller, *Phys. Rev. E* **52**, 2893 (1995).
- ¹⁹A. Laio and M. Parrinello, *Proceedings of the National Academy of Sciences* **99**, 12562 (2002), <http://www.pnas.org/content/99/20/12562.full.pdf>.
- ²⁰A. Barducci, M. Bonomi, and M. Parrinello, *Wiley Interdisciplinary Reviews: Computational Molecular Science* **1**, 826 (2011), <https://onlinelibrary.wiley.com/doi/pdf/10.1002/wcms.31>.
- ²¹E. Darve, D. Rodriguez-Gomez, and A. Pohorille, *The Journal of Chemical Physics* **128**, 144120 (2008), <https://doi.org/10.1063/1.2829861>.
- ²²J. Hénin, G. Fiorin, C. Chipot, and M. L. Klein, *Journal of Chemical Theory and Computation* **6**, 35 (2010), pMID: 26614317, <https://doi.org/10.1021/ct9004432>.
- ²³F. Pietrucci, *Reviews in Physics* **2**, 32 (2017).
- ²⁴A. C. Pan, T. M. Weinreich, Y. Shan, D. P. Scarpazza, and D. E. Shaw, *Journal of Chemical Theory and Computation* **10**, 2860 (2014), pMID: 26586510, <https://doi.org/10.1021/ct500223p>.
- ²⁵C. D. Fu, L. F. L. Oliveira, and J. Pfaendtner, *Journal of Chemical Theory and Computation* **13**, 968 (2017), pMID: 28212010, <https://doi.org/10.1021/acs.jctc.7b00038>.
- ²⁶H. Hotelling, *J. Educ. Psych.* **24** (1933).
- ²⁷R. T. McGibbon, B. E. Husic, and V. S. Pande, *The Journal of Chemical Physics* **146**, 044109 (2017), <https://doi.org/10.1063/1.4974306>.
- ²⁸A. Amadei, A. B. M. Linssen, and H. J. C. Berendsen, *Proteins: Structure, Function, and Bioinformatics* **17**, 412 (1993), <https://onlinelibrary.wiley.com/doi/pdf/10.1002/prot.340170408>.
- ²⁹K. P. F.R.S., *The London, Edinburgh, and Dublin Philosophical Magazine and Journal of Science* **2**, 559 (1901), pCA beginnings, <https://doi.org/10.1080/14786440109462720>.
- ³⁰J. M. Troyer and F. E. Cohen, *Proteins: Structure, Function, and Bioinformatics* **23**, 97 (1995), <https://onlinelibrary.wiley.com/doi/pdf/10.1002/prot.340230111>.
- ³¹W. Härdle and L. Simar, *Applied Multivariate Statistical Analysis* (Springer Berlin Heidelberg, 2007).

- ³²M. Ceriotti, G. A. Tribello, and M. Parrinello, Proceedings of the National Academy of Sciences **108**, 13023 (2011), <http://www.pnas.org/content/108/32/13023.full.pdf>.
- ³³J. B. Tenenbaum, V. d. Silva, and J. C. Langford, Science **290**, 2319 (2000), <http://science.sciencemag.org/content/290/5500/2319.full.pdf>.
- ³⁴M. A. Rohrdanz, W. Zheng, M. Maggioni, and C. Clementi, The Journal of Chemical Physics **134**, 124116 (2011), <https://doi.org/10.1063/1.3569857>.
- ³⁵M. Balasubramanian and E. L. Schwartz, Science **295**, 7 (2002), <http://science.sciencemag.org/content/295/5552/7.full.pdf>.
- ³⁶D. L. Donoho and C. Grimes, Proceedings of the National Academy of Sciences **100**, 5591 (2003), <http://www.pnas.org/content/100/10/5591.full.pdf>.
- ³⁷H. Risken and T. Frank, *The Fokker-Planck Equation: Methods of Solution and Applications (Springer Series in Synergetics)* (Springer, 1996).
- ³⁸R. R. Coifman, S. Lafon, A. B. Lee, M. Maggioni, B. Nadler, F. Warner, and S. W. Zucker, Proceedings of the National Academy of Sciences **102**, 7426 (2005), <http://www.pnas.org/content/102/21/7426.full.pdf>.
- ³⁹R. R. Coifman, S. Lafon, A. B. Lee, M. Maggioni, B. Nadler, F. Warner, and S. W. Zucker, Proceedings of the National Academy of Sciences **102**, 7432 (2005), <http://www.pnas.org/content/102/21/7432.full.pdf>.
- ⁴⁰R. R. Coifman and S. Lafon, Applied and Computational Harmonic Analysis **21**, 5 (2006), special Issue: Diffusion Maps and Wavelets.
- ⁴¹B. Nadler, S. Lafon, R. R. Coifman, and I. G. Kevrekidis, Applied and Computational Harmonic Analysis **21**, 113 (2006), special Issue: Diffusion Maps and Wavelets.
- ⁴²R. R. Coifman, I. G. Kevrekidis, S. Lafon, M. Maggioni, and B. Nadler, Multiscale Modeling & Simulation **7**, 842 (2008), <https://doi.org/10.1137/070696325>.
- ⁴³M. A. Rohrdanz, W. Zheng, B. Lambeth, J. Vreede, and C. Clementi, PLOS Computational Biology **10**, 1 (2014).
- ⁴⁴W. Zheng, A. V. Vargiu, M. A. Rohrdanz, P. Carloni, and C. Clementi, The Journal of Chemical Physics **139**, 145102 (2013), <https://doi.org/10.1063/1.4824106>.
- ⁴⁵F. Noé and F. Nüske, Multiscale Modeling & Simulation **11**, 635 (2013), <https://doi.org/10.1137/110858616>.
- ⁴⁶J. McCarty and M. Parrinello, The Journal of Chemical Physics **147**, 204109 (2017), <https://doi.org/10.1063/1.4998598>.

- ⁴⁷F. Noé and C. Clementi, *Journal of Chemical Theory and Computation* **11**, 5002 (2015), pMID: 26574285, <https://doi.org/10.1021/acs.jctc.5b00553>.
- ⁴⁸F. Noé, R. Banisch, and C. Clementi, *Journal of Chemical Theory and Computation* **12**, 5620 (2016), pMID: 27696838, <https://doi.org/10.1021/acs.jctc.6b00762>.
- ⁴⁹M. Duan, J. Fan, M. Li, L. Han, and S. Huo, *Journal of Chemical Theory and Computation* **9**, 2490 (2013).
- ⁵⁰M. I. Jordan, ed., *Learning in Graphical Models* (MIT Press, Cambridge, MA, USA, 1999).
- ⁵¹M. Schöberl, N. Zabaras, and P.-S. Koutsourelakis, *Journal of Computational Physics* **333**, 49 (2017).
- ⁵²L. Felsberger and P. Koutsourelakis, *Communications in Computational Physics* (accepted, 2018), arXiv:1802.03824.
- ⁵³D. P. Kingma and M. Welling, “Auto-encoding variational bayes,” (2013), arXiv:1312.6114.
- ⁵⁴D. J. Rezende, S. Mohamed, and D. Wierstra, in *Proceedings of the 31th International Conference on Machine Learning, ICML 2014, Beijing, China, 21-26 June 2014* (2014) pp. 1278–1286.
- ⁵⁵S. Kmiecik, D. Gront, M. Kolinski, L. Wieteska, A. E. Dawid, and A. Kolinski, *Chemical Reviews* **116**, 7898 (2016), pMID: 27333362, <https://doi.org/10.1021/acs.chemrev.6b00163>.
- ⁵⁶W. G. Noid, J.-W. Chu, G. S. Ayton, and G. A. Voth, *The Journal of Physical Chemistry B* **111**, 4116 (2007), pMID: 17394308, <https://doi.org/10.1021/jp068549t>.
- ⁵⁷M. S. Shell, *The Journal of Chemical Physics* **129**, 144108 (2008), <https://doi.org/10.1063/1.2992060>.
- ⁵⁸C. Peter and K. Kremer, *Soft Matter* **5**, 4357 (2009).
- ⁵⁹J. Trashorras and D. Tsagkarogiannis, *SIAM Journal on Numerical Analysis* **48**, 1647 (2010).
- ⁶⁰E. Kalligiannaki, M. A. Katsoulakis, P. Plech, and D. G. Vlachos, *Journal of Computational Physics* **231**, 2599 (2012).
- ⁶¹I. Bilionis and N. Zabaras, *The Journal of Chemical Physics* **138**, 044313 (2013), <https://doi.org/10.1063/1.4789308>.
- ⁶²J. F. Dama, A. V. Sinitskiy, M. McCullagh, J. Weare, B. Roux, A. R. Dinner, and G. A. Voth, *Journal of Chemical Theory and Computation* **9**, 2466 (2013), pMID: 26583735,

<https://doi.org/10.1021/ct4000444>.

- ⁶³W. G. Noid, The Journal of Chemical Physics **139**, 090901 (2013), <https://doi.org/10.1063/1.4818908>.
- ⁶⁴T. T. Foley, M. S. Shell, and W. G. Noid, The Journal of Chemical Physics **143**, 243104 (2015), <https://doi.org/10.1063/1.4929836>.
- ⁶⁵M. Langenberg, N. E. Jackson, J. J. de Pablo, and M. Müller, The Journal of Chemical Physics **148**, 094112 (2018), <https://doi.org/10.1063/1.5018178>.
- ⁶⁶C. X. Hernández, H. K. Wayment-Steele, M. M. Sultan, B. E. Husic, and V. S. Pande (2017).
- ⁶⁷C. Wehmeyer and F. Noé, The Journal of Chemical Physics **148**, 241703 (2018), <https://doi.org/10.1063/1.5011399>.
- ⁶⁸M. M. Sultan, H. K. Wayment-Steele, and V. S. Pande, Journal of Chemical Theory and Computation **14**, 1887 (2018), pMID: 29529369, <https://doi.org/10.1021/acs.jctc.8b00025>.
- ⁶⁹M. J. Beal, *Variational Algorithms for Approximate Bayesian Inference*, Ph.D. thesis, Gatsby Computational Neuroscience Unit, University College London (2003).
- ⁷⁰B. J. Alder and T. E. Wainwright, The Journal of Chemical Physics **31**, 459 (1959).
- ⁷¹D. Landau and K. Binder, *A Guide to Monte Carlo Simulations in Statistical Physics* (Cambridge University Press, New York, NY, USA, 2005).
- ⁷²Y. LeCun, Y. Bengio, and G. Hinton, Nature **521**, 436 EP (2015).
- ⁷³Z. Ghahramani, Nature **521**, 452 EP (2015).
- ⁷⁴W. von der Linden, V. Dose, and U. von Toussaint, *Cambridge University Press* (Cambridge University Press, 2014) p. 649.
- ⁷⁵A. Y. Ng and M. I. Jordan, in *Advances in Neural Information Processing Systems 14*, edited by T. G. Dietterich, S. Becker, and Z. Ghahramani (MIT Press, 2002) pp. 841–848.
- ⁷⁶D. J. C. MacKay, *Information theory, inference, and learning algorithms* (Cambridge University Press, 2003).
- ⁷⁷C. Bishop, in *Learning in Graphical Models* (MIT Press, 1999) p. 371403.
- ⁷⁸A. Cichocki and S.-i. Amari, Entropy **12**, 1532 (2010).
- ⁷⁹S.-H. Cha, “Comprehensive survey on distance/similarity measures between probability density functions,” (2007).
- ⁸⁰Inference on the generalized α -divergence is addressed in Ref. [?].

- ⁸¹D. J. C. MacKay, *Neural Comput.* **4**, 448 (1992).
- ⁸²A. Gelman, C. Robert, N. Chopin, and J. Rousseau, “Bayesian data analysis,” (1995).
- ⁸³E. T. Jaynes, *The Mathematical Intelligencer* **27**, 83 (2005).
- ⁸⁴M. D. Hoffman, D. M. Blei, C. Wang, and J. Paisley, *J. Mach. Learn. Res.* **14**, 1303 (2013).
- ⁸⁵R. Ranganath, S. Gerrish, and D. M. Blei, “Black box variational inference,” (2013), arXiv:1401.0118.
- ⁸⁶J. W. Paisley, D. M. Blei, and M. I. Jordan, in *ICML* (2012).
- ⁸⁷A. P. Dempster, N. M. Laird, and D. B. Rubin, *Journal of the Royal Statistical Society. Series B (Methodological)* **39**, 1 (1977).
- ⁸⁸R. M. Neal and G. E. Hinton (MIT Press, Cambridge, MA, USA, 1999) Chap. A View of the EM Algorithm That Justifies Incremental, Sparse, and Other Variants, pp. 355–368.
- ⁸⁹T. M. Ruiz, Francisco JR and D. Blei, in *Advances in neural information processing systems* (2016) pp. 460–468.
- ⁹⁰P. Zhao and T. Zhang, “Accelerating minibatch stochastic gradient descent using stratified sampling,” (2014), arXiv:1405.3080.
- ⁹¹D. P. Kingma and J. Ba, “Adam: A method for stochastic optimization,” (2014), arXiv:1412.6980.
- ⁹²P.-A. Mattei and J. Frellsen, “Leveraging the exact likelihood of deep latent variable models,” (2018), arXiv:1802.04826.
- ⁹³N. Metropolis, A. W. Rosenbluth, M. N. Rosenbluth, A. H. Teller, and E. Teller, *The Journal of Chemical Physics* **21**, 1087 (1953), <https://doi.org/10.1063/1.1699114>.
- ⁹⁴W. K. Hastings, *Biometrika* **57**, 97 (1970).
- ⁹⁵L. L. Cam, *International Statistical Review / Revue Internationale de Statistique* **58**, 153 (1990).
- ⁹⁶M. West, in *Bayesian Statistics* (Oxford University Press, 2003) pp. 723–732.
- ⁹⁷M. A. Figueiredo and S. Member, *IEEE Transactions on Pattern Analysis and Machine Intelligence* **25**, 1150 (2003).
- ⁹⁸D. J. C. MacKay and R. M. Neal, “Automatic relevance determination for neural networks,” Tech. Rep. (University of Cambridge, 1994).
- ⁹⁹M. E. Tipping, *J. Mach. Learn. Res.* **1**, 211 (2001).

- ¹⁰⁰H. Ritter, A. Botev, and D. Barber, in *International Conference on Learning Representations* (2018).
- ¹⁰¹P. E. Smith, The Journal of Chemical Physics **111**, 5568 (1999), <https://doi.org/10.1063/1.479860>.
- ¹⁰²J. Hermans, Proceedings of the National Academy of Sciences **108**, 3095 (2011), <http://www.pnas.org/content/108/8/3095.full.pdf>.
- ¹⁰³G. Ramachandran, C. Ramakrishnan, and V. Sasisekharan, Journal of Molecular Biology **7**, 95 (1963).
- ¹⁰⁴R. Vargas, J. Garza, B. P. Hay, and D. A. Dixon, The Journal of Physical Chemistry A **106**, 3213 (2002), <https://doi.org/10.1021/jp013952f>.
- ¹⁰⁵S. P. Carmichael and M. S. Shell, The Journal of Physical Chemistry B **116**, 8383 (2012), pMID: 22300263, <https://doi.org/10.1021/jp2114994>.
- ¹⁰⁶E. J. Sorin and V. S. Pande, Biophys J **88**, 2472 (2005).
- ¹⁰⁷A. J. DePaul, E. J. Thompson, S. S. Patel, K. Haldeman, and E. J. Sorin, Nucleic Acids Res **38**, 4856 (2010).
- ¹⁰⁸M. P. Allen and D. J. Tildesley, *Computer Simulation of Liquids* (Clarendon Press, New York, NY, USA, 1989).
- ¹⁰⁹A. Onufriev, D. Bashford, and D. A. Case, Proteins: Structure, Function, and Bioinformatics **55**, 383 (2004), <https://onlinelibrary.wiley.com/doi/pdf/10.1002/prot.20033>.
- ¹¹⁰W. C. Still, A. Tempczyk, R. C. Hawley, and T. Hendrickson, Journal of the American Chemical Society **112**, 6127 (1990).
- ¹¹¹H. Berendsen, D. van der Spoel, and R. van Drunen, Computer Physics Communications **91**, 43 (1995).
- ¹¹²E. Lindahl, B. Hess, and D. van der Spoel, Molecular modeling annual **7**, 306 (2001).
- ¹¹³D. V. D. Spoel, E. Lindahl, B. Hess, G. Groenhof, A. E. Mark, and H. J. C. Berendsen, Journal of Computational Chemistry **26**, 1701 (2005), <https://onlinelibrary.wiley.com/doi/pdf/10.1002/jcc.20291>.
- ¹¹⁴B. Hess, C. Kutzner, D. van der Spoel, and E. Lindahl, Journal of Chemical Theory and Computation **4**, 435 (2008).
- ¹¹⁵S. Pronk, S. Pli, R. Schulz, P. Larsson, P. Bjelkmar, R. Apostolov, M. R. Shirts, J. C. Smith, P. M. Kasson, D. van der Spoel, B. Hess, and E. Lindahl, Bioinformatics **29**, 845 (2013).

- ¹¹⁶S. Páll, M. J. Abraham, C. Kutzner, B. Hess, and E. Lindahl, in *Solving Software Challenges for Exascale*, edited by S. Markidis and E. Laure (Springer International Publishing, Cham, 2015) pp. 3–27.
- ¹¹⁷M. J. Abraham, T. Murtola, R. Schulz, S. Pll, J. C. Smith, B. Hess, and E. Lindahl, *SoftwareX* **1-2**, 19 (2015).
- ¹¹⁸D. E. Rumelhart, G. E. Hinton, and R. J. Williams (MIT Press, Cambridge, MA, USA, 1986) Chap. Learning Internal Representations by Error Propagation, pp. 318–362.
- ¹¹⁹C. Van Der Malsburg, in *Brain Theory*, edited by G. Palm and A. Aertsen (Springer Berlin Heidelberg, Berlin, Heidelberg, 1986) pp. 245–248.
- ¹²⁰S. Haykin, *Neural Networks: A Comprehensive Foundation*, 2nd ed. (Prentice Hall PTR, Upper Saddle River, NJ, USA, 1998).
- ¹²¹D. J. Rezende and S. Mohamed, “Variational inference with normalizing flows,” (2015), arXiv:1505.05770.
- ¹²²D. P. Kingma, T. Salimans, R. Jozefowicz, X. Chen, I. Sutskever, and M. Welling, “Improving variational inference with inverse autoregressive flow,” (2016), arXiv:1606.04934.
- ¹²³G. Klambauer, T. Unterthiner, A. Mayr, and S. Hochreiter, in *Advances in Neural Information Processing Systems 30*, edited by I. Guyon, U. V. Luxburg, S. Bengio, H. Wallach, R. Fergus, S. Vishwanathan, and R. Garnett (Curran Associates, Inc., 2017) pp. 971–980.
- ¹²⁴W. Humphrey, A. Dalke, and K. Schulten, *Journal of Molecular Graphics* **14**, 33 (1996).
- ¹²⁵A. M. Fluitt and J. J. de Pablo, *Biophysical Journal* **109**, 1009 (2015).
- ¹²⁶Y. Sugita and Y. Okamoto, *Chemical Physics Letters* **314**, 141 (1999).
- ¹²⁷Y. Zhou, A. Kloczkowski, E. Faraggi, and Y. Yang, *Prediction of Protein Secondary Structure*, Methods in Molecular Biology (Springer New York, 2016).
- ¹²⁸I. J. Goodfellow, J. Pouget-Abadie, M. Mirza, B. Xu, D. Warde-Farley, S. Ozair, A. Courville, and Y. Bengio, “Generative adversarial networks,” (2014), arXiv:1406.2661.
- ¹²⁹Y. Saatchi and A. G. Wilson, (2017), arXiv:1705.09558.
- ¹³⁰T. Salimans, I. Goodfellow, W. Zaremba, V. Cheung, A. Radford, X. Chen, and X. Chen, in *Advances in Neural Information Processing Systems 29*, edited by D. D. Lee, M. Sugiyama, U. V. Luxburg, I. Guyon, and R. Garnett (Curran Associates, Inc., 2016) pp. 2234–2242.
- ¹³¹R. Galvelis and Y. Sugita, *Journal of Chemical Theory and Computation* **13**, 2489 (2017), pMID: 28437616, <https://doi.org/10.1021/acs.jctc.7b00188>.